Production of Direct Photons in Lead–Lead Collisions

Production of Direct Photons in Lead–Lead Collisions

Productie van directe fotonen in botsingen tussen loodkernen

(met een samenvatting in het Nederlands)

Proefschrift
ter verkrijging van de graad van doctor
aan de Universiteit Utrecht
op gezag van de rector magnificus prof. dr. J. C. Stoof
ingevolge het besluit van het college voor promoties
in het openbaar te verdedigen
op dinsdag 23 oktober 2007 des middags te 14.30 uur

door

Eugène Christiaan van der Pijll
geboren op 31 juli 1974 te Amersfoort

Promotor: Prof. dr. R. Kamermans

Co-promotor: Dr. N.J.A.M. van Eijndhoven

Contents

Chapter 1

Introduction and conclusions

One of the hot topics in the field of high-energy physics of the last few years has been the search for the Quark–Gluon Plasma (QGP). This "new" state of matter only occurs at very high temperatures, and can only be produced experimentally in collisions of heavy ions at high energy.

In chapter 2, the properties of the QGP will be discussed. This discussion includes a number of phenomena that have been used to obtain information from this short-living state. One of these probes consists of direct photons, which are produced in the earliest and hottest phases of heavy-ion collisions. The production of these photons is highly dependent on the temperature of the system, and therefore they provide an opportunity to study the thermal evolution of the collisions. There have already been a number of experiments on most of the QGP probes, including the direct photons. The results of these experiments are also presented. These provide an indication, but not more than that, of the presence of a QGP in the most recent heavy-ion collision experiments.

Chapter 3 is dedicated to the WA98 experiment. One of the aims of WA98, located at the SPS facility, was to study Pb-Pb collisions at 158 A GeV. Amongst the detectors in WA98, which are described in chapter 3, is a large photon spectrometer. This is the main instrument that we have used in the search for the direct photon signal.

The most important part of this thesis can be found in chapter 4. First, a description is given of our method of analysis of the photon signal. This is based on a comparison of events of various centralities. The remaining part of the chapter shows the outcome of this procedure.

In the fifth chapter, a theoretical model is presented, which predicts the yield of direct photons from thermal processes in the QGP and in a hadron gas for a system of colliding heavy-ion nuclei. A comparison of these theoretical

predictions and our experimental result shows that they are comparable, for some reasonable choices of parameters for the evolution of the system.

1.1 Main conclusions

These are the most important results of the study presented here. The support for these results can be found in chapter 4 and 5 of this thesis.

Direct photons have been observed for the first time in the p_T interval where thermal emission may be dominant. Properly, the signal we have derived from the experiments is a lower limit for the direct photon yield in the most central events. Assuming that the direct photon emission in our more peripheral events is negligible, which seems reasonable, the central direct photon spectrum is equal to this lower limit. Our results nicely agree with the earlier results from WA98 at higher p_T, and at lower p_T, they are compatible with the upper limits from the same study.

The combined results from our analysis and the earlier WA98 study cannot be described by thermal emission only; the parameters that would have to be chosen for the thermal evolution of the system would be highly unrealistic. A good description can be obtained if, next to the thermal emission from a hadron gas and the Quark-Gluon Plasma, also contributions from nucleon-nucleon collisions are taking into account. The observed spectrum can be explained by a system with an initial temperature of 205 MeV and a formation time of the equilibrated system of 1 fm/c. In this model, the thermal photon component dominantly arises from an equilibrated hadronic system, although contributions from non-equilibrium processes cannot be excluded.

Our experimental results are also in good agreement with recent more detailed calculations.

Chapter 2

The Quark Gluon Plasma

2.1 The structure of matter

2.1.1 Ordinary nuclear matter

The structure of matter at low temperature is well known. All substances around us consist of atoms or ions. The first experiments that examined the inner structure of atoms were performed in the early twentieth century by Rutherford. He discovered the atomic nucleus from the scattering of α-particles on atoms. From similar experiments, it was possible to calculate the size of the nucleus.

In later years, scattering experiments were performed at ever higher energies. These revealed the substructures of the nucleus, leading to the so-called Standard Model. This model describes quarks and leptons, the elementary particles that make up all matter, as well as the intermediary particles that carry the interactions, the gauge bosons.

The lightest and most common lepton is the electron. In ordinary matter, most electrons are bound to atoms by the electromagnetic force, but they can be isolated easily. In contrast, quarks have never been found in isolation, but only in hadronic particles containing two or more quarks. This is because of the nature of the strong force, which grows in strength when the distance increases. The only stable configurations of quarks are those with no net strong-force charge, so called colourless configurations. Each quark can have one of three colours, with anti-quarks having corresponding anti-colours. The simplest possible colourless hadrons are therefore the mesons (a quark–anti-quark pair) and the baryons (containing three quarks or three anti-quarks of all three colours).

The most common quarks are the up and down quarks, the lightest quarks, with a mass of at most a few MeV. These quarks form protons and neutrons, the

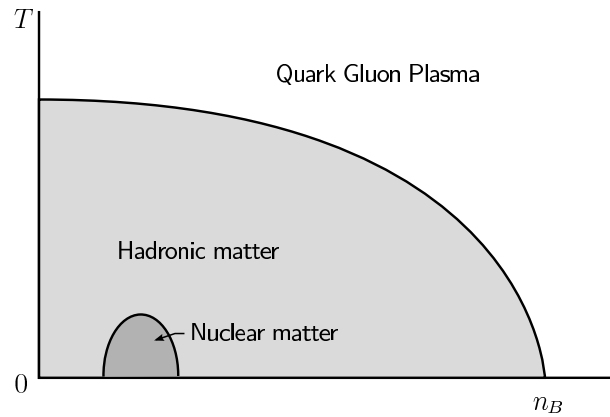

Figure 2.1: The phase diagram of nuclear matter

building blocks of atomic nuclei. These nucleons consist of three valence quarks, which are embedded in a sea of virtual quark–anti-quark pairs and held together by gluons, the gauge bosons of the strong force. In a simplified model of the nucleon, the constituent quarks and gluons are free to move around inside the nucleon, because the strong force is relatively feeble at short distances. However, when the distance between the quarks becomes larger, the coupling increases. This leads to so-called string fragmentation, when the binding energy between the quarks is enough to create new quark–anti-quark pairs. In this way, instead of isolating the original quarks, new hadronic particles are produced. Therefore, no quarks can be found in isolation. This is known as confinement.

2.2 Deconfined matter

The properties of nuclear matter can be described by an equation of state, which relates temperature, pressure and density. As long as the conditions stay reasonably close to those in atomic nuclei, the change in behaviour of the constituent particles is only gradual. However, if for example the energy density in a nucleus is raised above a certain critical level, current theory predicts a phase transition. This transition can be compared to the transition between the liquid and the gas phase of a drop of water.

The phase diagram of nuclear matter is shown in figure 2.1. This diagram describes the properties of the quarks and gluons as a function of temperature

and net baryon density, assuming thermal equilibrium. The net baryon density is defined as

$$n_B = \frac{1}{3}(n_q - n_{\bar{q}}), \tag{2.1}$$

where n_q and $n_{\bar{q}}$ are the total quark and anti-quark densities respectively, summed over all quark flavours. In a baryon-free environment, with net baryon density zero, there is an equal number of quarks and anti-quarks.

At low temperature and net baryon density, quarks and gluons in nuclear matter are confined, as described in the previous section. At these low temperatures, the quarks are combined into hadrons, which are bound together into nuclei. At higher temperatures the hadrons are no longer bound to nuclei. This phase is called the hadron gas. The composition of this gas will depend on the circumstances. The ratio of baryons (three quarks or anti-quarks) to mesons (a quark–anti-quark pair), for example, depends heavily on the net baryon density, and the temperature mainly determines the ratio of light and heavy hadrons. These ratios follow directly from thermodynamical models.

As shown in figure 2.1, the temperature and net baryon density of a hadron gas cannot increase indefinitely. At a certain point, a phase transition occurs. Crossing this phase transition, hadrons are unable to hold together, and they lose their identity. The quarks and gluons, which were confined in the hadrons at lower energies, are now free to move through the whole system. This phase transition is analogous to the break-down of an atomic gas at high temperatures into a plasma of ions and free electrons. The new state of nuclear matter is therefore known as the Quark–Gluon Plasma (QGP). In the QGP, the quarks are deconfined. Of course, this does not mean that these quarks can be isolated: when they leave the plasma, they will no longer be deconfined, and they will become a part of a hadron, for example through string fragmentation.

To obtain a QGP, either the temperature or the net baryon density of ordinary nuclear matter has to be increased, or both. It is expected that a QGP state exists in the centre of neutron stars. These are burned-out stars with a mass of a few times the solar mass and a diameter of around 10km. Because of the high pressure inside these stars, they consist almost entirely of neutrons. In the centre of the stars, the neutron density is so high that the neutrons overlap and lose their identity. In this way, a QGP can be formed even at a low temperature.

In nuclear collision experiments both the temperature and n_B increase. When the energy of the colliding nuclei is high enough, the high temperature and baryon density will result in deconfinement. This creation of a QGP has been the aim of a number of experiments. In the next section, an extensive description of these heavy-ion experiments is given.

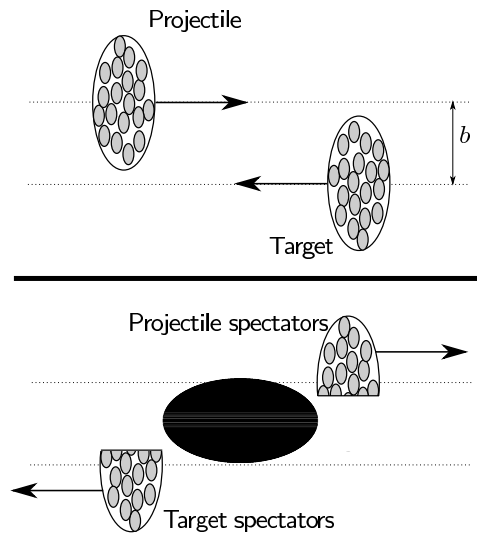

Figure 2.2: Two phases of a heavy-ion collision.

2.3 Examining the QGP

2.3.1 Heavy-ion collisions

Our main source of experimental data about the equation of state of nuclear matter is the heavy-ion experiments at accelerators like the Super Proton Synchotron (SPS) at CERN and the Relativistic Heavy-Ion Collider (RHIC) at Brookhaven National Laboratory. There are several reasons why heavy-ion collisions provide the best oppportunity to study the QGP. It is possible to reach high momenta in accelerators, and therefore a high energy density in a collision. Because of the large size of heavy ions, this high energy density can be maintained in a relatively large volume long enough to obtain a thermal equilibrium at a temperature which is comparable to that necessary for the phase transition. In a collision of protons or other light atomic nuclei, the energy released in the collision can escape the collision zone much easier, which reduces the probability of creating a QGP considerably.

Figure 2.2 shows a collision of two lead nuclei in the centre-of-momentum (c.m.s.) system. Because of the high velocity of the nuclei, they are Lorentz contracted to disks along the direction of motion. In the collision, the nucleons loose some of their energy. This energy forms a fireball, which expands to fill the

space between the nuclei after the collision. In this fireball, particles are formed in thermal processes. The most important are the quarks and the gluons, which form a QGP if the energy density is high enough.

The collision in figure 2.2 is off-centre. Therefore, not all the nucleons of the two colliding nuclei are participating. The impact parameter b is defined as the distance between the trajectories of the nuclei before the collision. If $b = 0$, the centres of the nuclei collide, and in the case of equal sized nuclei, all nucleons are participants. In this case the collision is called *central*. Collisions with large b are called *peripheral*. In peripheral collisions there are many nucleons which are not affected by the collision. These spectator nucleons keep the same velocity as before the collision. On the other hand, the participants lose some of their energy and the direction of their motion is in general changed. This means that the centrality of a collision can be derived by detecting the number of nucleons that remain close to the beam axis with approximately their initial energy.

The number of reactions at a certain centrality is expressed in terms of an invariant cross section. The total cross section of the collision, σ, is a measure of the probability of an inelastic collision, analogous to the cross section in Rutherford's experiments. Another useful quantity is the invariant differential cross section, $Ed^3\sigma/dp^3$. It is an invariant measure of the probability of a collision between two nuclei. The minimum bias cross section, $\sigma_{\text{min bias}}$, represents that part of the total cross section that is accessible via experimental measurements. Every impact parameter range corresponds to a fraction of the total cross section. When dividing collision events into centrality classes, we will often express these classes in terms of the cross section. For example, we will use a selection of the most central events corresponding to 10% of the minimum bias cross section in our analysis.

Most of the current information about the equation of state of nuclear matter comes from fixed-target experiments at the SPS accelerator at CERN. At this facility, the highest beam energy that could be reached for lead nuclei was 158A GeV, representing 158 GeV per nucleon. This corresponds to a collision energy of about 18 GeV per nucleon–nucleon collision in the c.m.s. frame.

The most recent experimental information has been obtained at the RHIC facility in Brookhaven. This is a collider, which means that the available energy in a collision can be much higher than at the SPS. The highest possible c.m.s. energy per nucleon-nucleon collision at the RHIC is 200 GeV for gold ion beams.

In the first half of 2008, the Large Hadron Collider (LHC) at CERN is scheduled to start operation. Most of the time, the LHC will be used for proton–proton collisions, but there are also heavy-ion runs planned. The c.m.s. energy available in these collisions will reach 5.5 TeV per nucleon–nucleon collision.

According to our current understanding of the equation of state of nuclear matter, a QGP will easily be obtained under these conditions in all central collisions. One of the experiments that is being built for the LHC, Alice, is specifically designed for the detection and detailed investigation of the QGP. The experiments at the LHC are expected to increase our knowledge of the nuclear equation of state tremendously.

2.3.2 The signatures of a QGP

The Quark Gluon Plasma can only be detected indirectly by measuring its particle production. It is too short-living and covers too little volume to be measured directly. However, the production of a number of particles is influenced by the deconfined state of quarks and gluons in a QGP. The production rate of these particles can be measured, and any deviations from the 'normal' production rates at high energy collisions can be a signal for QGP formation.

Another way to detect the formation of a QGP is to look at the thermal evolution of the system. After the collision of two nucleons, the temperature of the created system immediately begins to drop. If the initial temperature is high enough to create a QGP, the system will pass through a phase transition during the cooling. During this phase transition, the system is a mixture of a QGP and a hadron gas, at more or less a constant temperature (depending on the order of the phase transition). The effect of such a plateau in the temperature evolution can be detected in the spectrum of thermally produced particles.

The following effects are examples of signals of the QGP:

- J/ψ suppression;
- heavy quark enhancement;
- thermal dileptons;
- direct photons.

None of these process is generally considered to be a definite indication of the presence of a Quark-Gluon Plasma on its own. It is the combination of several, preferably simultaneous, measurements that can prove the existence of the QGP.

J/ψ suppression

The J/ψ particle is a bound state of a c and a $\bar{c}$ quark. This meson has a large mass, 3097 MeV. The J/ψ particles that are measured in collision experiments originate mostly from hard scattering interactions in the earliest stages of the

collisions between nuclei. After a J/ψ particle has been produced, it may leave the collision area, and decay. From the decay products, the presence of the J/ψ can be detected experimentally. However, there are some processes that destroy the J/ψ particle before it has left the system. For example, it may interact with a nucleon, leading to a breakup of the J/ψ:

$$J/\psi + N \rightarrow D + \bar{D}. \tag{2.2}$$

Because of this and other reactions, a fraction of the J/ψ particles is absorbed.

In a Quark Gluon Plasma, there is an additional method that suppresses the measured production rate of J/ψ particles. Because of the presence of unconfined coloured particles (quarks and gluons), a c quark will have a polarizing effect: the quark attracts anti-quarks and gluons from the surrounding region. The effective colour charge of both the c and the $\bar{c}$ is lowered by this effect, which is similar to the electromagnetic Debye effect. This lowers the attractive force between the constituent particles of the J/ψ. Because the bonding between the c and $\bar{c}$ is much weaker in the QGP, the J/ψ particle has a higher probability to dissolve in the medium. As c quarks are much less abundant than u or d quarks because of their high mass, the loose c and $\bar{c}$ quarks are unlikely to recombine into a J/ψ again, and they will end up as 'open charm', for example in D mesons The measured production of J/ψ mesons will therefore be suppressed if a QGP is formed.

A J/ψ suppression effect has been measured in the NA50 experiment at the CERN-SPS. The number of muon pairs produced in J/ψ decay was compared to the spectrum of muon pairs produced by the Drell-Yan process. The Drell-Yan cross-section grows predictably with the number of nucleon–nucleon collisions, so this comparison is a good way to find the J/ψ suppression. The NA50 experimental data in figure 2.3 show a drop in the J/ψ production for the most central events of about 25%, compared to the results for peripheral events and the results of theoretical calculations.

However, because of the uncertain quality of the models of J/ψ suppression due to other processes, and of the computation of the Drell-Yan cross-section in these most central collisions, this result does not prove the existence of a QGP by itself.

Strange quark enhancement

A second effect that is predicted to occur in a Quark-Gluon Plasma is the enhancement of the production of heavy quarks. As the energy density and/or net baryon density in the QGP is high, the effective mass of the strange quarks

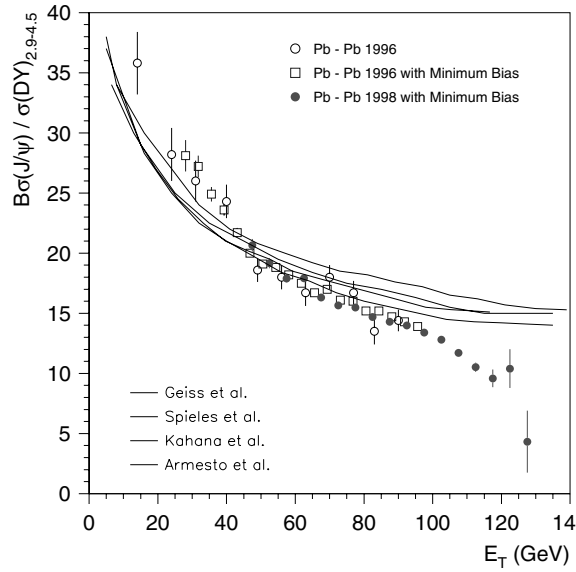

Figure 2.3: J/ψ production in the NA50 experiment [1]. The curves show the outcome of several theoretical models. At high transverse energy E_T, corresponding to the most central events, the observed J/ψ yield is clearly lower than expected from the models.

is lowered. The lowered mass difference between the various quark flavours results in a higher relative production of s quarks, which can be observed as a higher number of K mesons and baryons like Λ and Ξ.

The best current results on heavy quark production come from the WA97 and NA57 experiments. These SPS experiments have measured strange particle production rates for heavy ion collisions at various beam energies and centralities. When the number of produced particles is compared to the number of nucleons participating in the collision, earlier results for p–A experiments showed consistent results for various target nucleons from Be to Pb. However, in central Pb–Pb collisions, the measured production of strange hadrons is enhanced, as shown in figure 2.4. This enhancement grows with the number of strange quarks in the particles, up to an enhancement by a factor of about 15 for $\Omega^- + \bar{\Omega}^+$. This is consistent with the higher production of strange quarks that is expected in a QGP.

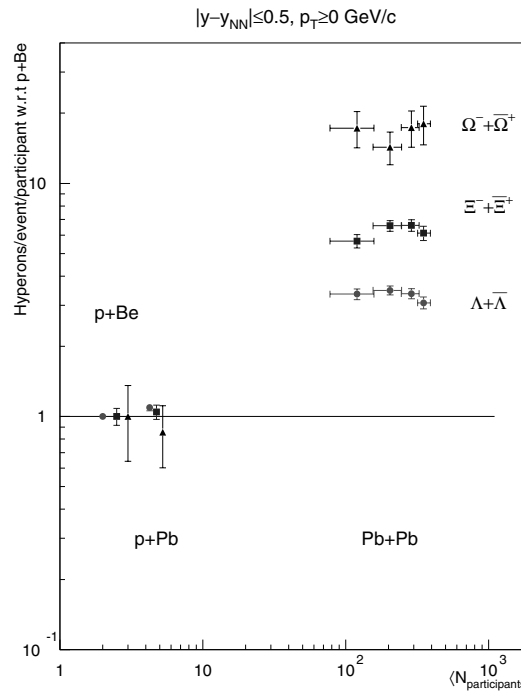

Figure 2.4: Strange particle production in the NA57 experiment [2]. The production of the Λ, Ξ and Ω baryons, which contain one or more strange quarks, is clearly enhanced in collisions with a high number of participating nucleons, compared to the light-ion collsions with a low number of participants.

Thermal signals

Another sign of the presence of a QGP can be given by the thermal production of di-leptons, caused by quark and gluon collisions. Di-leptons are also produced in in later, cooler stages of a collision, and therefore the mere presence of di-leptons is not a signal of the formation of a QGP. However, the di-lepton spectrum depends strongly on the thermal evolution of the system. An analysis of the spectral shape will result in information about the conditions in the early stages of the reaction, which can give an indication about the possibility of a QGP having formed.

An interaction between a quark and an anti-quark can produce a virtual photon, which can decay in a lepton and an anti-lepton. This is a thermal

process: the total energy of the lepton pair depends on the energy distribution of the quarks in the medium. After the system has cooled down, the constituent quarks will have been bound into separate hadrons. Interactions between these hadrons also produce lepton pairs, in a similar way and in similar quantities as in the QGP. The only difference between the di-lepton production in these two phases of the collision is the temperature of the medium.

To draw conclusions about the nature of the system, and to prove the existence of a QGP, the observed rate of lepton pairs has to be compared to theoretical predictions, based on calculated production rates and models for the thermodynamical evolution of the system. The presence of a phase transition, when the temperature is more or less constant, changes the outcome of these models. By comparing the experimental results to models with or without a phase transition, the presence of the QGP can be deduced. If a QGP is present in an early phase of a collision, the phase transition to a hadron gas will show up in the temperature evolution as a phase of constant temperature.

Similarly, the production of direct photons also depends on the thermodynamical conditions in the medium. Like the dileptons, direct photon production depends on the temperature. A possible phase transition can be detected after an analysis of the observed photon spectrum. This will be discussed in more detail in chapter 5.

2.4 WA98 Direct photon result

A direct photon signal from heavy-ion collisions has been measured for the first time in the WA98 experiment [3]. In the following chapters, the data from this experiment will be used for an alternative method of analysis [4], which enables an extension of the investigation into the low p_T regime. Unlike the high p_T domain, which is dominated by photons from hard initial scattering, the low p_T regime contains mainly thermal photons. In this section, the earlier analysis of the WA98 data will be described in short. Later, we will compare the results described in this section with the direct photon spectrum from our own method, which is the main subject of this thesis.

The direct photon signal which has been obtained was produced in the collisions of two lead nuclei at a beam energy of 158GeV per nucleon (158AGeV). The experimental set-up of the WA98 experiment will be described in detail in chapter 3. The most important detectors for the purpose of measuring the direct photon signal are a large photon spectrometer and a calorimeter measuring transverse energy produced in the collisions. The signal of the latter detector was used to divide the events into centrality classes as described in section

2.3.1. The analysis was performed for two centrality classes. The class with the highest centrality corresponds to the central class in our later analysis, as described in section 4.2.

2.4.1 Background reduction

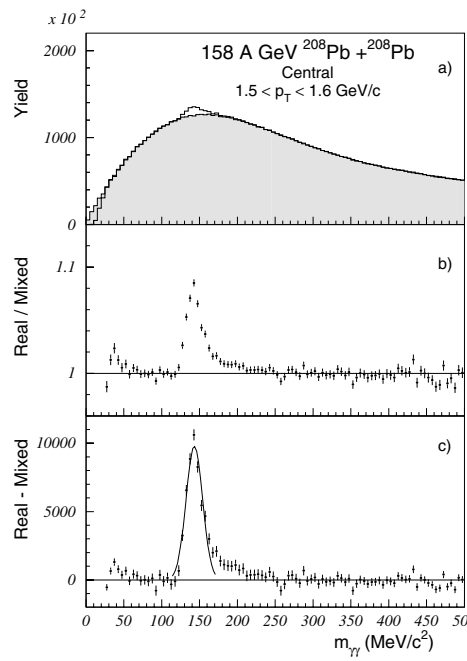

Figure 2.5: The two-photon invariant mass spectrum for central events [3]. In part a) the shaded part of the histogram shows the mixed-event invariant mass distribution, with the real-event distribution as an open histogram. Part b) shows the ratio of the mass distributions for real and mixed events. Part c) shows the difference of both distributions

The main problem in measuring a direct photon signal is the large background of decay photons from neutral mesons, mainly π^0. To remove this background, an invariant mass analysis of photon pairs was performed on the photon spectrometer signals. For every two photons in a single event, the invariant mass

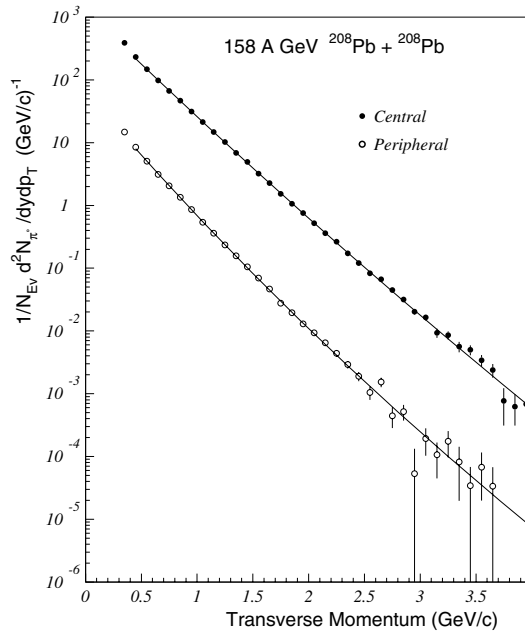

Figure 2.6: The π^0 transverse momentum distribution for central and peripheral events [3]. Only statistical errors are shown.

of that pair was calculated:

$$M_{\gamma\gamma} = \sqrt{2E_1E_2(1-\cos\phi)}, \tag{2.3}$$

where E_1 and E_2 are the energies of the photons and ϕ is the opening angle. For a pair of photons originating in the decay of a π^0, $M_{\gamma\gamma}$ should be equal to the π^0 mass. The number of photon pairs per event is very high, but only a very small fraction of these combinations represent a genuine π^0. The acceptance region of the photon detector only covers a relatively small part of the entire spatial angle, so for most π^0 decays, at most one of the photons is detected. This means that the π^0 spectrum will have to be corrected for detector acceptance effects. Even if both photons from a π^0 are detected, this correct combination will be swamped by the combinatorial background, which consists of combinations of one of these photons with one of the possibly hundreds of other detected photons.

The two-photon invariant mass spectrum, containing a peak of correct combinations at the π^0 mass and a very large combinatorial background, is then compared to an invariant mass spectrum from mixed events. This spectrum is obtained by taking two photons from two different events. These photons cannot come from the same π^0, and the resulting invariant mass spectrum will not contain a π^0 peak. The number of π^0's is found by subtracting the mixed-event spectrum from the one-event invariant mass spectrum. The two events that are mixed should be chosen with care. If the characteristics of the events, for example the multiplicity of the photon signals, differ too much, the constructed background photon pairs will have different properties from the photon pairs in the real events.

To apply this construction method for the π^0 background, the assumption

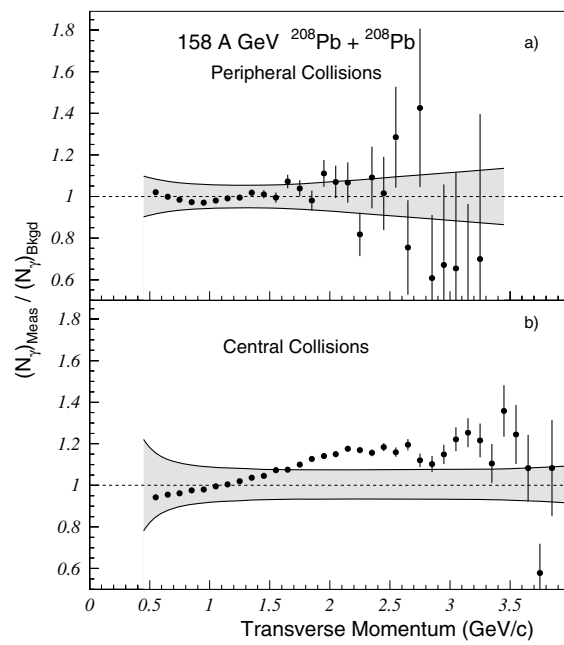

Figure 2.7: The ratio of measured photons and background photons [3]. The error bars show statistical errors. The shaded bands indicate the systematic errors.

has to be made that the π^0's within an event are not significantly correlated. If there is such a correlation within an event, for example because of HBT correlations, this will affect the two-photon invariant-mass spectrum of the real events. Two mesons in two different events will of course not be correlated. The relative position of their decay photons will therefore be distributed randomly, and the mixed-event invariant-mass spectrum will not be the same as the combinatorial background in the real events. It is likely that any correlations between pions are very small. However, as the combinatorial background is very large in comparison to the π^0 signal, small systematic correlations can have a large effect on the measured signal.

In figure 2.5 the result is shown for one p_T interval. The contents of the π^0 peak can be obtained by fitting the difference of the mixed and real-event invariant mass distributions by a Gaussian. This results in the number of π^0's in that particular p_T interval. By repeating this for several p_T values, a π^0 p_T spectrum can be obtained. This spectrum then has to be corrected for acceptance and efficiency effects. The final result of this analysis is shown in figure 2.6. The contributions of other neutral meson spectra were obtained by m_T scaling. Only the yield of the η meson could be determined experimentally by a two-photon invariant mass analysis similar to the one outlined above. This could be done only for central events in a restricted p_T range.

The background decay photon spectrum can be calculated from the neutral meson spectra, and compared to the measured photon spectrum. Figure 2.7 shows the ratio of the measured photon count and the expected photon count due to decay photons. In peripheral events no significant direct photon production was observed, but in central events the photon spectrum shows a significant excess for $p_T > 1.5\,\mathrm{GeV}$. The direct photon spectrum resulting from the invariant-mass analysis is shown in figure 2.8.

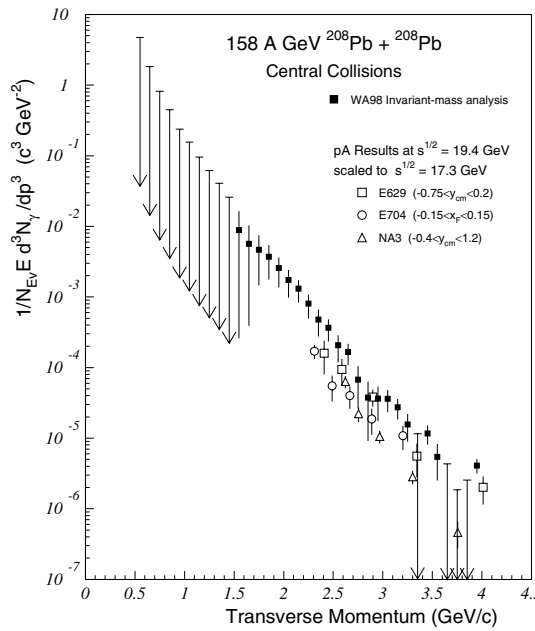

Figure 2.8: The direct photon spectrum, determined with the invariant-mass background reduction method [3].

Chapter 3

The WA98 experiment

The aim of the WA98 experiment [5] is to study heavy-ion collisions by means of a simultaneous measurement of electromagnetic and hadronic signals in a large acceptance region. A brief description of the overall setup is given in section 3.1. The detectors that will be used in the present analysis will be discussed in more detail in section 3.2 and 3.3.

3.1 Experimental setup

Figure 3.1 shows the configuration of the detectors as used during the collection of the data set which is used in the analysis described in this thesis. The beam, coming from the left in figure 3.1, consists of fully stripped ^{208}Pb nuclei. These have been accelerated to an energy of 158A GeV by the CERN Super Proton Synchotron (SPS).

Several targets have been used during the various run periods, including a niobium and a nickel target. However, the present analysis is performed on data obtained with a single target, consisting of a lead foil with a thickness of 239 mg/ cm^2. As the total geometrical inelastic cross section of lead–lead collisions is about 6.2 barn, the probability of an interaction for this target is about 0.4% per incoming lead nucleus. Additionally, some data were taken without a target present, to provide information about the background interactions of the lead beam particles with non-target nuclei, e.g. remnant gas nuclei in the beam pipe.

A system of colliding lead nuclei is symmetric, which ensures absence of centrality dependent rapidity shifts. In a system of two unequal colliding nuclei the c.m.s. of the total system can be different from the c.m.s. of the interacting parts of the nuclei. For example, in a central collision of two unequal nuclei all nucleons in the smaller nucleus participate in the collision, but a ring of outer

nucleons of the larger nucleus would be spectators, that is, they would not participate. As the ratio of participants from both nuclei varies as a function of the centrality of the collisions, the centre-of-momentum system of a collison is also centrality-dependent. This complicates the analysis of the experimental results and the comparison of the results for different centrality classes. These complications are not present in a symmetrical colliding system, as the numbers of participants from both nuclei are equal for all centralities.

Mid-rapidity for the lead–lead collisions at an incident beam energy of $158A$ GeV is at a pseudo-rapidity value of $\eta = 2.9$ in the laboratory frame, and the c.m.s. energy per nucleon–nucleon collision is $\sqrt{s} = 17.3\,\mathrm{GeV}$.

A number of trigger detectors, located at a short distance upstream of the target, were employed during data-taking. One of these, a quartz plate detector 3.5 m upstream of the target, was used as a start counter. This detector is based on the Čerenkov radiation produced by a traversing beam particle. As the intensity of Čerenkov light produced by a particle with charge Z scales with Z^2, events originating from beam particles other than lead nuclei can be ignored by imposing thresholds on the signal of the start counter. A scintillator counter was used to veto particles from the beam halo, and a scintillator detector at 2.7m upstream of the target detected particles from beam interactions upstream of the target, including those in the start counter. These three detectors, which identify the incoming particles and define clean interaction conditions, were one part of the WA98 trigger system. The MIRAC and ZDC detectors, which will be discussed later, were the other part of the trigger.

The Plastic Ball detector [6] consisted of 655 scintillator modules capable of identifying low-energy charged particles. These modules were placed spherically around the target, providing a pseudo-rapidity coverage of $-1.7 < \eta < 1.3$. With this detector, observations in the target fragmentation region can be made. In addition, this detector allows determination of the reaction plane, which enables e.g. flow analysis [7].

The Silicon Drift Detector (SDD) and the Silicon Pad Multiplicity Detector (SPMD) were located inside the Plastic Ball, 12.5 cm and 30 cm downstream of the target, respectively. These detectors measured the charged particle multiplicity in the rapidity region of about $2.5 < \eta < 3.75$.

A large dipole magnet providing 1.6 Tm bending power allowed for momentum measurement and identification of charged particles in two tracking arms [8]. The magnetic field of this magnet was in the vertical (y) direction, so that the bending plane for magnetic particles was the horizontal ($x - -z$) plane. In the standard magnetic field configuration the negative particles were deflected towards the right tracking arm (looking downstream from the target). This

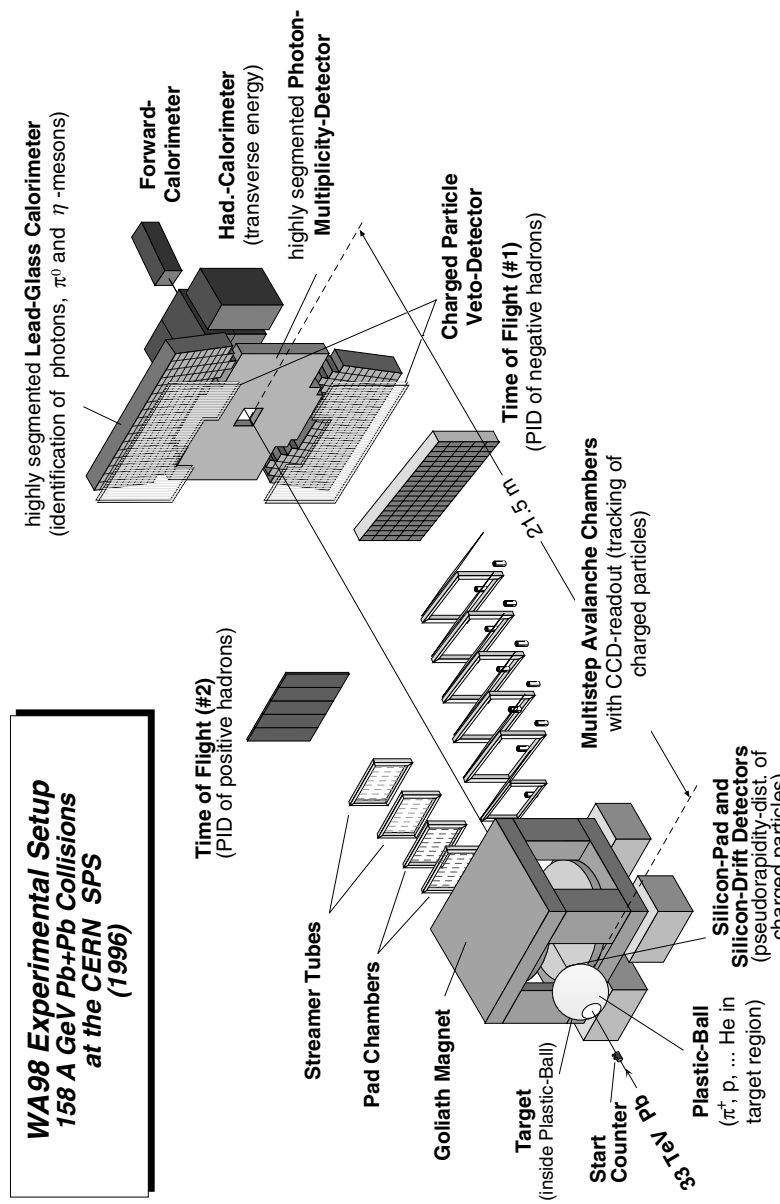

Figure 3.1: The detector set-up of the WA98 experiment.

arm consisted of six multi-step avalanche chambers. The second arm, which measured the positive particle tracks, was only installed during the 1996 run, and consisted of two multi-step avalanche chambers similar to those in the first arm, and of two streamer tube [9] tracking chambers.

The high resolution Photon Multiplicity Detector (PMD) [10] covered the interval $2.8 < \eta < 4.4$, and was located at 21.5 m from the target. This detector consisted of a 1.7 cm thick lead converter in front of a matrix of 54,000 $2 \times 2 \times 0.3\,\mathrm{cm}^3$ scintillator pads. The PMD measured the photon multiplicity, but little information about the energy of the photons can be extracted from the signals, because electromagnetic showers are not contained in this pre-shower detector, which has a thickness of only 3.3 radiation lengths.

Located behind the PMD, the Mid-Rapidity Calorimeter (MIRAC) [11] and the Zero-Degree Calorimeter (ZDC) [12] measured the transverse energy and the forward energy respectively. These quantities give an indication of the centrality of a collision.

The ZDC (located in the beamline behind the MIRAC detector) consisted of 35 modules with dimensions $15 \times 15 \times 270\,\mathrm{cm}^3$. Each module consisted of 148 lead/scintillator sandwich layers. The particles that ended up in the ZDC were the fragments of the beam nuclei which had not interacted with the target nuclei. For the most central events, the ZDC measured an energy of at most a few TeV, whereas in grazing collisions most of the 33 TeV of the incoming nucleus was detected.

The MIRAC detector, shown in figure 3.2, was located at 25 metres downstream of the target. It consisted of 180 modules with a cross sectional area of $20 \times 20\,\mathrm{cm}^2$, and a length of 214 cm, placed parallel to the beam line. Each module was divided into a lead-scintillator electromagnetic sector followed by an iron-scintillator hadronic section, and was read out with a photomultiplier at each end. The module signals were weighted and summed to provide the total transverse energy in the pseudo-rapidity region $3.2 < \eta < 5.4$.

The MIRAC detector was used in the trigger system to identify valid events and to classify them according to centrality. A low threshold on the MIRAC signal was used to measure the minimum bias event rate. Two additional thresholds were imposed somewhat above and far above the minimum bias threshold. These three MIRAC thresholds define three event classes[1], which together correspond to the entire minimum bias cross section. The most peripheral of these classes, between the two lowest thresholds, contained about 20% of the minimum bias events, and the most central class, above the highest threshold,

[1]These classes are not identical to the centrality classes used in our analysis, as described in section 4.2

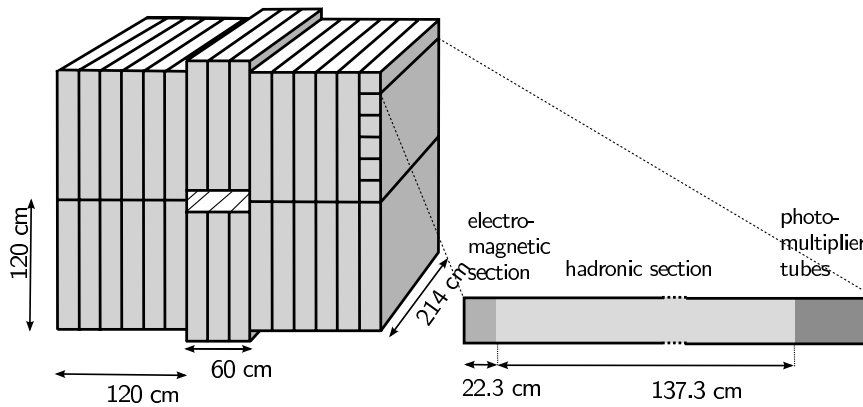

Figure 3.2: The mid-rapidity calorimeter (MIRAC). Left: front view of the entire stack. Right: side view of a single tower.

contained about the 10% most central events.

As the event rate was higher than the maximum possible data acquisition rate, the peripheral and the not-so-central classes were typically downscaled by a factor of 4 and 16 respectively.

3.2 The photon spectrometer

The most important detector for our purposes is the Lead-glass Detector Array (LEDA), depicted in figure 3.3. This calorimeter was located at 21.5 m downstream of the target, and consisted of 10,080 seperate modules. Together, these modules covered a large part of the pseudo-rapidity range $2.4 < \eta < 3.0$, near mid-rapidity ($\eta_m = 2.9$).

Each module consisted of a $4 \times 4 \times 40 \mathrm{cm}^3$ block of TF1-type lead-glass, which consists of glass loaded with a high fraction of lead-oxide. Electromagnetic particles entering a module start an electromagnetic cascade (shower), resulting in the emission of Čerenkov light. This light was collected by photomultipliers at the back of each module.

Figure 3.2 shows a supermodule, consisting of 24 lead-glass modules. Each supermodule had a gain monitoring system mounted on the front of the detector [13]. The output of this system was used to correct the module signals for

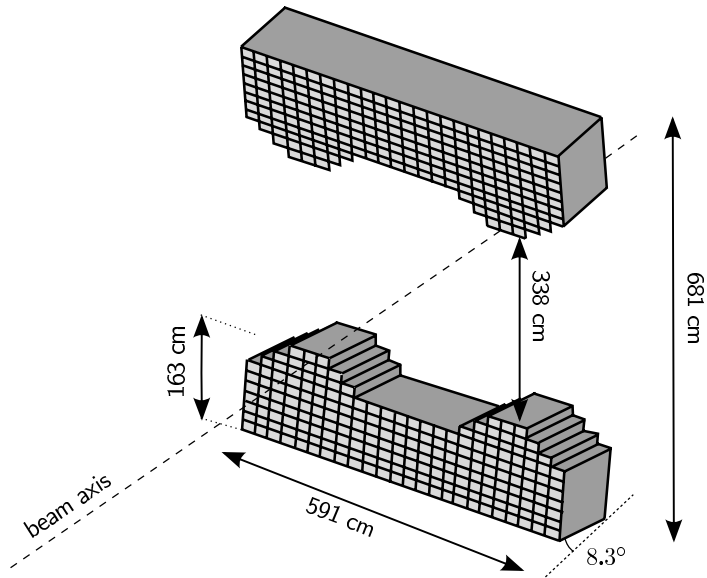

Figure 3.3: The configuration of the Leadglas Detector Array (LEDA).

gain variations. These variations are caused by a number of effects, for example variations in temperature and photomultiplier high voltage, and radiation damage in the lead-glass. The monitoring system consisted of three LEDs of different wavelengths. The emitted light of these LEDs was distributed by a reflective cover onto the lead-glass modules, while the intensity of the LEDs was monitored by a photodiode mounted on top of the cover on the front of the modules.

In beam tests, the energy resolution of the LEDA calorimeter was found to be:

$$\frac{\sigma_E}{E} = 10^{-2}\left(1.4 + \frac{5.8}{\sqrt{E}}\right), \tag{3.1}$$

and the measured spatial resolution of the lead-glass modules was

$$\sigma_{x,y} = \left(0.4 + \frac{7.1}{\sqrt{E}}\right) \text{ mm}, \tag{3.2}$$

where E is the energy of the incoming particle in GeV.

In our analysis, we will calculate the transverse energy of the incoming photons. In first approximation, the transverse energy is given by:

$$E_T = E \sin\theta \approx E \tan\theta = E \cdot R/z, \tag{3.3}$$

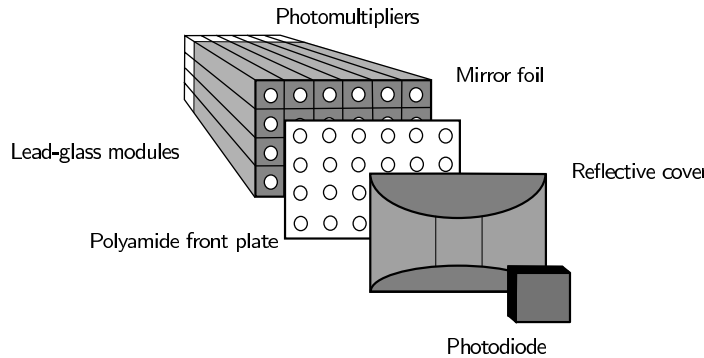

Figure 3.4: The components of a LEDA supermodule.

where θ is the angle of the photon trajectory with the beam axis, R is the distance from the calorimeter hit to the beam axis, and z is the distance to the interaction point at the target along the beam axis. The resolution of R is of the same order of magnitude as the spatial resolution given in (3.2). For typical values of R (say 5m) and E (between 0.5 GeV and 3 GeV), the relative resolution of R is in the order of 10^{-3}. This is an order of magnitude smaller than the relative energy resolution (3.1), which shows that the energy resolution is the limiting factor in our later analysis.

3.2.1 Electromagnetic showers

In a simple, one-dimensional model of electromagnetic cascades [14], photons convert into electron-positron pairs, whereas electrons and positrons lose energy because of bremsstrahlung. In this way, after each interaction the number of particles doubles and the average energy per particle halves. When the energy of an electron or positron drops below the critical energy ε of the medium, the energy loss because of ionization starts to dominate the effect of bremsstrahlung. After this limit is reached, all shower particles dissipate their energy through ionization and excitation.

The mean free path between two interactions in the cascade is energy-independent for particle energies above 100 MeV. This characteristic distance, called the radiation length X_0, depends only on the properties of the medium. The length of the shower is determined by the high-energy interactions, and

scales with X_0. It is therefore convenient to express the dimensions of electromagnetic calorimeters in terms of X_0.

For the TF1 modules used in the WA98 experiment, the radiation length is 2.8 cm, which means that the total length of a module is 14.4 radiation lengths. Most of the energy in an electromagnetic shower will be dissipated after 5 to 10 radiation lengths, and the shower produced by an incoming photon or electron will therefore be largely contained in the detector.

The particles that are produced in the cascade will not be traveling in exactly the same direction as the original particle. As a consequence, the shower will grow both in the transverse and in the longitudinal direction. The signals associated with one incoming particle can therefore be detected in the photomultipliers of several neighbouring modules. In order to reconstruct the total shower energy the signals of the individual modules have to be clustered, which is performed according to the procedure outlined in section 3.2.3

3.2.2 Hadronic showers

When hadrons interact in a medium, they can also initiate a shower. However, the processes involved are different from those in electromagnetic showers, and the showers which are formed have some distinct features.

Incoming hadrons can start cascades through their strong interactions with the medium. Typically, these reactions give multiple particles with fairly large transverse momenta. However, in a dense medium the cross section for this process is smaller than for the electromagnetic cascade process. The interaction length, defined as the mean free path between two inelastic interactions, has a value of $\lambda_h = 38$ cm for the TF1 lead-glass used in our spectrometer. This is only slightly less than the length of the modules of our detector. Only part of the shower is therefore contained in the detector, and the true energy of incoming hadronic particles cannot be determined in the lead-glass calorimeter.

As λ_h is of the same order as the thickness of the detector, many of the hadrons will pass through the detector without initiating a cascade. However, these particles will be detected because of their energy loss due to ionization processes and Čerenkov radiation. This energy loss, dE/dx, is well described by the Bethe-Bloch formula [15], which shows that this loss is almost independent of the type of incoming particle. Although dE/dx depends on the velocity of the particle, most hadrons will have a velocity where the dE/dx is close to its minimum. The spectrum of deposited energy of these particles, the so-called minimum ionizing particles (MIP's), will therefore be sharply peaked at a relatively low energy deposit.

3.2.3 Clustering

As described in the previous two sections, many showers created in the photon spectrometer are not contained in one lead-glass module, but spread to neighbouring modules. This means that the individual module signals cannot be used to determine the energy of the incoming particles. Before the total shower signals can be analysed, neighbouring signals have to be clustered.

After clustering, each module can only be part of one shower. To ensure this, all modules are ordered depending on their signals. The clustering procedure starts at the module with the highest signal. The energies of all modules in a 5×5 square around this starting module are summed, and a cluster is created at the location of the central module. This procedure is repeated for the other modules in which a signal has been detected, except for those modules of which the signal is already contained in a cluster.

When an energetic particle enters the lead-glass calorimeter near the edge, it is possible that the created shower is not completely contained in the detectors. To prevent this from having an effect on the measured spectra, the modules on the edge of the detector are not used as the centre of a cluster. However, when a cluster is started at a neighbouring position, the energy of the edge module is added to the shower energy.

The LEDA detector contained a number of defective modules. These modules showed a non-linear response with respect to incoming energy, and these signals were ignored in the clustering process. Modules neighbouring these bad modules were treated as if they were edge modules: although their signals were used in clustering, no cluster could be started having such a module at the centre.

3.3 Charged Particle Veto

Although many of the charged hadrons that enter the spectrometer show up in the so-called MIP peak, a considerable fraction still shows a signal comparable to that of low energy photons. Also, the showers that are started by electrons or positrons are very similar to those started by photons, as both types of cascades are formed by the same processes. Therefore, a Charged Particle Veto (CPV) detector was placed in front of the lead-glass calorimeter [16]. This detector is placed about 50 cm from the LEDA surface, and covers its total acceptance region.

The CPV consisted of two sections, as indicated in figure 3.1, each containing 86 Iarocci-type streamer tubes [9] in a single layer. These streamer tubes were

placed vertically, and were filled with a mixture of 10% argon, 30% isobutane and 60% carbon dioxide.

When a charged particle passes through a tube, it produces an electrical discharge in the gas mixture. This charge is detected via charge induction by one of the more than 49,000 pads mounted on the outside of the tube. Each pad had a size of 7 mm in the horizontal direction, which was thebending plane of the magnet, and 42 mm in the vertical direction.

The signals of the CPV detector are used in our analysis to tag the charged particles that are detected in the lead-glass calorimeter. This procedure is described in section 4.3.1.

Chapter 4

Analysis and experimental results

The experimental data of the WA98 experiment have resulted in the first measurement of direct photons in heavy-ion collisions, as shown in section 2.4. However, only an upper limit could be given for the direct photon yield in the low $p_\perp$ range.

In section 4.1, an alternative analysis method will be presented, which enables an actual measurement of the direct photon yield in the thermal regime. The following sections will address the application of this method to the WA98 data, and the result of the analysis will be given in section 4.8.

4.1 Inclusive photon analysis method

The analysis described in section 2.4 has resulted in a direct photon spectrum at $p_\perp > 1.5\,\mathrm{GeV}/c$. At lower $p_\perp$ values, the systematic errors inherent to the method are too large to extract a reliable signal, and therefore only upper limits were given in that $p_\perp$ region. However, extension of the measured signal to lower $p_\perp$ is important, because it is in this region that a thermal signal is most likely to be found [17]. Furthermore, photon production due to hard initial scattering obscures the thermal signal at high $p_\perp$ values. Consequently, a different method of analysis is required to obtain the direct photon yield for $p_\perp < 1.5\,\mathrm{GeV}/c$.

The approach that will be presented in this section is based on inclusive photon yields, and has the important advantages of having less dependence on Monte Carlo models and instrumental effects. This allows the extraction of a direct photon signal at lower $p_\perp$, enabling the study of the thermal regime.

To apply this analysis method, the measured events are divided into two classes of centrality. By a proper scaling of the inclusive photon spectrum of

the peripheral events to the central one, the spectrum of the hadronic decay photons, which is the background of the direct photon signal, can be estimated. The basic measurements that are required for the analysis are the inclusive photon yield as a function of momentum for both the central and the peripheral event classes, denoted by $\mathrm{Cen}_\gamma(p)$ and $\mathrm{Per}_\gamma(p)$ respectively, and the corresponding π^0 spectra $\mathrm{Cen}_{\pi^0}(p)$ and $\mathrm{Per}_{\pi^0}(p)$.

Both E and $p_\perp$ spectra can be used in the analysis. Either choice has its advantage: a direct photon spectrum resulting from an energy based analysis can be compared to the theoretical models presented in chapter 5 more easily, whereas a direct photon spectrum as a function of the transverse momentum can be directly compared to earlier experimental results. The general method described here does not depend on the variable that is chosen, and when the symbol p is used in the remainder of this section, it can denote either the particle energy E or the transverse momentum $p_\perp$. In the analysis based on particle energy, the measured spectra are of course dependent on the reference frame; the transverse momentum is invariant under frame shifts along the longitudinal axis (which is the axis of the collision).

Although the method as it is described here is based on the π^0 spectra, measurements of the charged pions could also be used, if the experimental set-up would allow this. According to [18], the yields of the π^0's and of the charged pions show the same centrality dependence. The π^+'s and the π^-'s can be measured directly, as opposed to neutral mesons, which have to be reconstructed from the two-photon invariant-mass distribution. However, because the data used in this analysis were obtained without a magnetic field, in this case the charged-pion spectra are not available, and the π^0 spectra are used to obtain the correct scaling factor.

As will be shown in Monte Carlo simulations (section 4.6, see also [4]) the ratio of the central and the peripheral yield of π^0's is approximately equal to that of their decay photons. Assuming that the much smaller decay photon contributions from η's and other resonances scale with the π^0's [19], and therefore have the same ratio, we obtain the equality:

$$\frac{\mathrm{Cen}_{\gamma h}}{\mathrm{Per}_{\gamma h}} = \frac{\mathrm{Cen}_{\pi^0}}{\mathrm{Per}_{\pi^0}} \equiv f(p), \tag{4.1}$$

where γh denotes the photons produced in hadronic decays and $f(p)$ represents an arbitrary function. Monte Carlo simulations and experimental results presented in later sections show that this $f(p)$ function is approximately constant. However, if this were not the case, the equality of the π^0 ratio and the γ ratio expressed in (4.1) would not hold.

The inclusive photon spectra Cen_γ and Per_γ consist of hadronic decay photons and direct photons (γd):

$$\mathrm{Cen}_\gamma = \mathrm{Cen}_{\gamma h} + \mathrm{Cen}_{\gamma d} \tag{4.2}$$

$$\mathrm{Per}_\gamma = \mathrm{Per}_{\gamma h} + \mathrm{Per}_{\gamma d} \tag{4.3}$$

Combined with the definition of $f(p)$, given in equation (4.1), these expressions lead to the following equation:

$$\mathrm{Cen}_\gamma - f(p) \cdot \mathrm{Per}_\gamma = \mathrm{Cen}_{\gamma d} - f(p) \cdot \mathrm{Per}_{\gamma d}. \tag{4.4}$$

In the derivation of equation (4.4), the hadronic decay photon spectra $\mathrm{Cen}_{\gamma h}$ and $\mathrm{Per}_{\gamma h}$ cancel, leaving only the direct photon spectra on the right hand side. The quantities on the left hand side, Cen_γ, Per_γ and $f(p)$, can all be measured directly. Therefore, this expression provides a good opportunity to study direct photon production in heavy-ion collisions.

Obviously, the result of the procedure is not the central direct photon yield, but a more complicated function of both the central and the peripheral direct photon spectrum. In general, the exact direct photon spectrum cannot be extracted using this method without knowledge of the relation between $\mathrm{Per}_{\gamma d}$ and $\mathrm{Cen}_{\gamma d}$. The presence of direct photons can however be proven, provided that the direct photon production does not scale with $f(p)$. Most theoretical models [17] indeed predict that the direct photon fraction of the total photon production grows rapidly with the number of interacting nucleons, and as such no scaling of the direct photon yield with $f(p)$ is expected.

The main reason for measuring the direct photon yield is the information it can provide about the conditions in the early phases of the collision. In particular, the temperature evolution of the initial phases determines both the shape of the spectrum and the absolute scale of the direct photon spectrum. Because our final result will not be a pure spectral shape, but a linear combination of two spectra, as defined in (4.4), we will not be able to draw conclusions about the temperature without making further assumptions about the dependence of the direct photon yield on centrality. Theory predicts a direct photon production which increases rapidly with the centrality of the collision, and in the earlier analysis of the WA98 data no signal was found for peripheral collisions [3]. In this case, equation (4.4) reduces to

$$\mathrm{Cen}_\gamma - f(p) \cdot \mathrm{Per}_\gamma = \mathrm{Cen}_{\gamma d}, \tag{4.5}$$

and consequently the direct photon spectrum for the central centrality class can be measured directly. Even if there is a small but significant peripheral

direct photon yield, the result of our analysis can be considered a lower limit of the central direct photon yield, and limits on the initial temperature can be extracted from both shape and absolute scale of the spectrum.

Using the assumption $\mathrm{Per}_{\gamma d} = 0$, the results of our analysis can be compared to the predictions of theoretical models, and conclusions about the evolution of the collision can be drawn. The validity of the above assumption is not straightforward for our analysis, as our peripheral event class is not the same as the one in the analysis described in section 2.4. However, even if the peripheral direct photon yield is measurably larger than 0, this will only reduce the central direct photon yield; the $\mathrm{Cen}_{\gamma d}$ that is obtained from the proposed procedure will then still be useful as a lower limit on the direct photon production. The comparison with the theoretical predictions will be discussed in section 5.

The inclusive photon analysis method we have described provides an opportunity to check the earlier WA98 direct photon spectrum and even to extend it to a different $p_\perp$ regime. Because our method is based on the ratio of the pion spectra for events of two centrality classes, a number of systematic uncertainties present in the earlier analysis will not be present here. With this difference in treatment of the photon background coming from hadronic decays, the error in our final result for the direct photon spectrum will differ from the previous result, which will hopefully mean that we can extend the measured direct photon spectrum to lower $p_\perp$ values.

The most important of these systematic effects removed by our analysis method are those connected with the absolute pion yield measurement. A systematic effect is for example introduced by defective modules in the lead-glass calorimeter. These modules reduce the acceptance of the calorimeter, and the size of this effect can change over time. However, the events in the two data sets in this analysis have been measured in the same runs. This means that the acceptance correction on the π^0 spectrum is the same for central and peripheral events measured in the same run. Consequently, these corrections will cancel in the central-to-peripheral ratio $f(p)$, which means that the time-dependent acceptance correction is not necessary.

Another effect is the background of neutron and anti-neutron signals in the calorimeter. This topic will be discussed in more detail in section 4.7.

4.2 Centrality based event classification

The centrality of the collisions can be characterized by a number of global observables, such as particle multiplicities, and forward and transverse energy. In our case, events were selected on basis of the total transverse energy in the

pseudo-rapidity range $3.7 < \eta < 5.5$, defined as the sum of the transverse energy of all the stacks of the MIRAC detector [11]:

$$E_T = \sum_i (E_T)_i = \sum_i E_i \sin\theta_i, \tag{4.6}$$

where the position of the stacks is described by the polar angles θ_i.

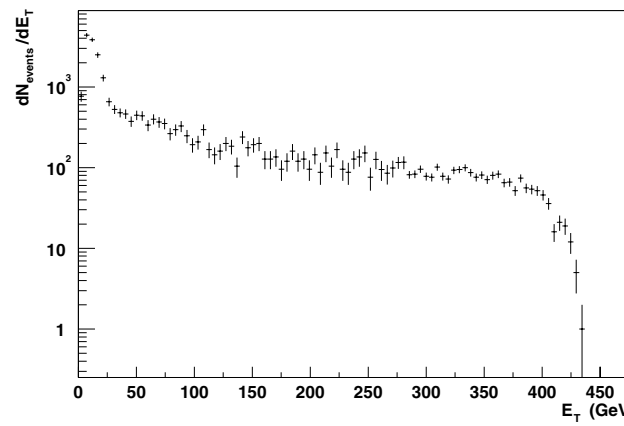

Figure 4.1: The E_T distribution for Pb+Pb collisions at 158A GeV beam energy. The vertical scale is arbitrary.

Figure 4.1 shows the E_T distribution for Pb+Pb collisions at 158A GeV beam energy. The high peak at low E_T consists of the most peripheral events. These are the grazing collisions with a low number of participating nucleons. At increasing centrality, the number of nucleons that are involved in the collision becomes higher, and the transverse energy that is produced gets larger. The most central collisions, with impact parameter b close to zero, have a total transverse energy of up to about 430 GeV.

Although the majority of the measured events are Pb+Pb collisions, there is a background of non-target interactions, including for instance interactions of the Pb beam with remnant gas nuclei in the beam pipe. To investigate this background, data have been taken without a target in place. The E_T distribution of these so called empty-target runs is presented in figure 4.2. In principle the photon spectrum can be corrected for the non-target interactions. To perform this correction, however, the overall normalisation of the non-target collisions should be known very accurately, to prevent the introduction of large systematic

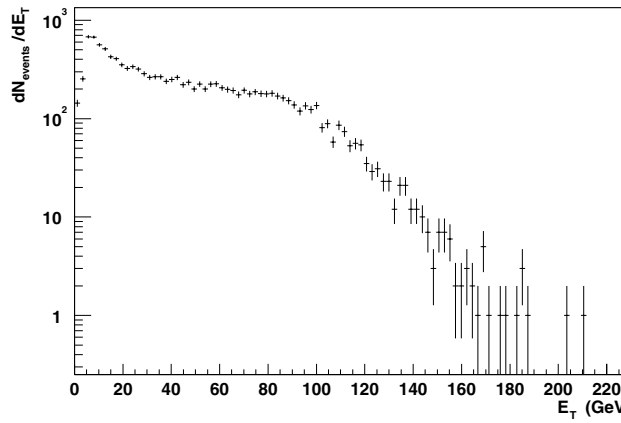

Figure 4.2: The E_T distribution for a magnet-on empty target run. The transverse energies are corrected for the effect of the magnetic field. The vertical scale is arbitrary.

uncertainties. As the goal of the analysis described here is to investigate the thermal $p_\perp$ regime, where systematic uncertainties dominate, we have chosen to eliminate the non-target effects instead of correcting for them. To achieve this, the lower E_T bound of the peripheral class should been chosen in such a way that most of the empty-target events fall below that value.

The available empty-target runs were performed with the GOLIATH magnet turned on. This has an effect on the total transverse energy: the average transverse energy of charged particles increases in the presence of a magnetic field. To correct for this effect, we compared the E_T distribution of a magnet-on run with a magnet-off run, The result of this comparison is that the magnetic field increases the total transverse energy produced in a collision by a factor of 1.12 ± 0.01. The horizontal scale of figure 4.2 has been corrected for this increase in E_T

The E_T limits of our central and peripheral classes are shown in table 4.1. These classes are equal to two of the centrality classes used in the invariant mass analysis described in section 2.4.

To calculate the fraction of events in our centrality classes originating in non-target interactions, we would need to know the relative scale of the two E_T distribution. Unfortunately, this fraction is not known accurately enough. However, we can compare the two distributions for transverse energies below

100 GeV. In this region, the total E_T distribution given in figure 4.1 provides an upper limit for the number of non-target interactions, and therefore also an upper limit of the relative normalization of the empty-target E_T distribution. For any E_T range, we can now determine an upper limit of non-target events.

For our choice of peripheral class, this upper limit on the contamination lies below 3%. This is a very generous upper limit, which assumes that all events with $E_T < 100$ GeV are from non-target interactions. The lower E_T limit of our central class lies well above the highest measured transverse energy in the empty-target run, so there is no need to account for this contamination for our central events.

	Central	Peripheral
Lower limit:		
E_T(GeV)	340	100
% $\sigma_{\text{min.bias}}$	6	41
b (fm)	4.6	9.2
Upper limit:		
E_T(GeV)	—	290
% $\sigma_{\text{min.bias}}$	—	10
b (fm)	0	5.8
$< N_{\text{part}} >$	336	143
N_{events}	3.24×10^5	3.06×10^5

Table 4.1: The definition of the centrality classes, based on the MIRAC-measured transverse energy. The upper and lower limits of both classes are given as E_T and as percentage of minimum bias events above that E_T.

The Glauber model of multiple-collision processes [20] can be used to describe a nucleus–nucleus collision in terms of collisions of the constituent nucleons. It relates the number of nucleon–nucleon collisions and the number of participating nucleons to the impact parameter b of the nucleus–nucleus collision. This model has been extended [21] to include the production of hadronic secondary particles in nucleon–nucleon collisions, which allows the calculation of measurable quantities such as the transverse energy E_T that is produced in a collision event [22]. Table 4.1 contains the impact parameters corresponding to the limits of our centrality classes, as well as the average number of participants.

4.3 Photon reconstruction and identification

4.3.1 Charged particle tagging

The Charged Particle Veto (CPV) detector, which is situated in front of the lead-glass calorimeter, makes it possible to identify the calorimeter signals that are produced by charged particles. This is important for the purity of the photon sample, which should be as high as possible in order to minimise systematic uncertainties arising from the charged particle contamination.

For every shower in the lead-glass calorimeter, the intersection of the particle trajectory with the plane of the CPV is calculated. This procedure is very simple for the data under investigation here, because of the absence of a magnetic field between the target and the CPV and LEDA detectors. Because of the size and position of the CPV, the calculated crossing point always falls within the acceptance of the CPV detector.

Figure 4.3 shows the distribution of distances between the projected LEDA hits and the actually recorded CPV hits. The concentration around $\Delta x = \Delta y = 0$ represents those combinations of lead-glass signals and CPV hits that are produced by the same particle. The LEDA hits of neutral particles are not correlated with CPV hits. This is seen in figure 4.3 and 4.4 as an approximately constant background of random correlations.

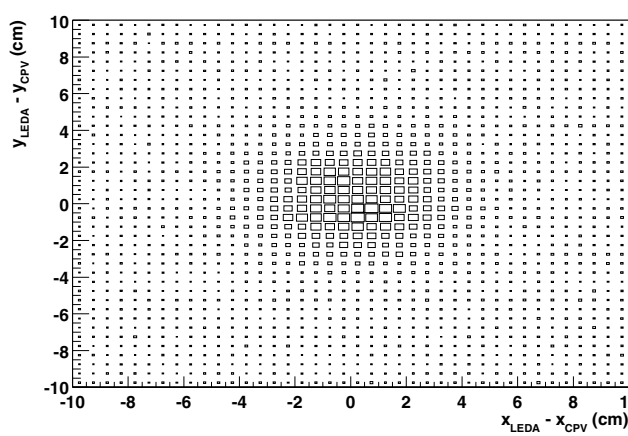

Figure 4.3: The distance from projected LEDA hits to their closest CPV hit.

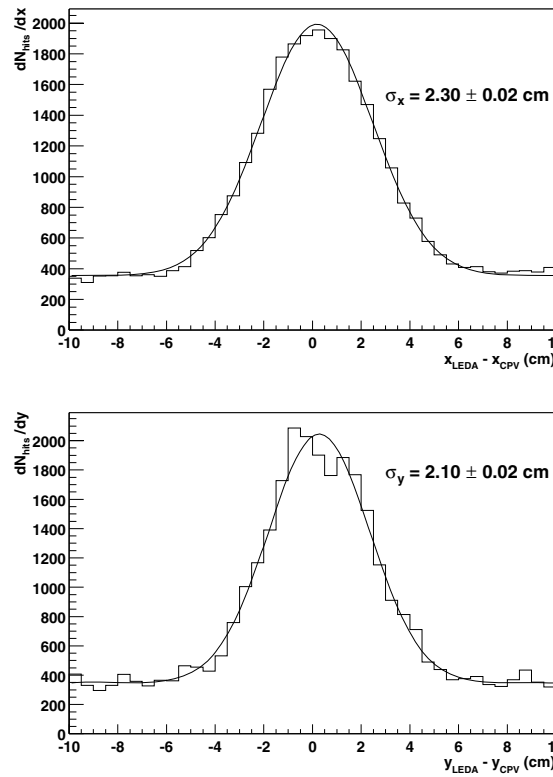

Figure 4.4: The x and y projections of the distance from projected LEDA hits to their closest CPV hit, corresponding to figure 4.3. The solid line represents the best fit for a Gaussion function plus a constant.

From figure 4.4 it is seen that the Δx and Δy peaks are approximately Gaussian, with $\sigma_x = 2.3$cm and $\sigma_y = 2.1$cm. These values for the distribution widths are compatible with the module size of the lead-glass detector and the pad size of the CPV, which provide a lower bound for the resolutions of the position measurements of the hits in both detectors.

For every LEDA hit, the confidence level of the matching of that hit with the closest CPV signal is determined. For the calculation of the confidence level, we determine a χ^2 value based on the observed distance between the actual CPV hit and the projected LEDA hit, taking into account the different peak widths

in the x and y direction:

$$\chi^2 = \sqrt{(\frac{\Delta x}{\sigma_x})^2 + (\frac{\Delta y}{\sigma_y})^2} \tag{4.7}$$

The confidence level is then given by:

$$\mathrm{CL}(\chi^2) = \int_{x>\chi^2} \frac{1}{2\pi} \exp(-x^2/2) dx. \tag{4.8}$$

The integrand of this expression is the distribution that χ^2 would have, if the distances between the projected LEDA and CPV hits would be Gaussian.

The shape of the confidence level distribution depends heavily on the nature of the sample. A sample of charged particles would show a Gaussian profile of Δx and Δy, which would correspond to a flat confidence level distribution. A sample of particles without a CPV hit, e.g. photons, shows only random correlations, corresponding to a flat Δx and Δy distribution (at least on distances smaller than the typical distance between CPV hits). This results in a confidence level distribution that is sharply peaked at 0 and falls to a constant value when CL goes to 1.

Figure 4.5 shows the general shape of a confidence level distribution as it can be obtained from the experimental results. It shows that the real situation is a superposition of the two cases outlined above. The high CL part of this plot can be described well with a constant function, representing the non-random correlations between CPV and projected LEDA hits. The area below the constant function is equal to the number of charged particles, detected by the CPV detector, while the part of the CL distribution above this line represent the random CPV–LEDA correlations (which contains the neutral particles, and a small contribution of charged particles that have not triggered the CPV detector).

This allows determination of the photon purity and charged particle contamination by introducing a confidence level threshold. Every entry above this CL cut is regarded as a charged particle, and is rejected, whereas every entry below the CL cut is accepted as a photon. The CL threshold (drawn as a vertical line in figure 4.5) and the fit at high CL (the horizontal line) divide the CL distribution in four parts, as indicated in the figure. The areas of these parts represent the following quantities:

A The number of accepted neutral particles, $N_{\mathrm{acc,neutr}}$.

B The number of rejected neutral particles, $N_{\mathrm{rej,neutr}}$.

C The number of accepted charged particles, $N_{\mathrm{acc,ch}}$.

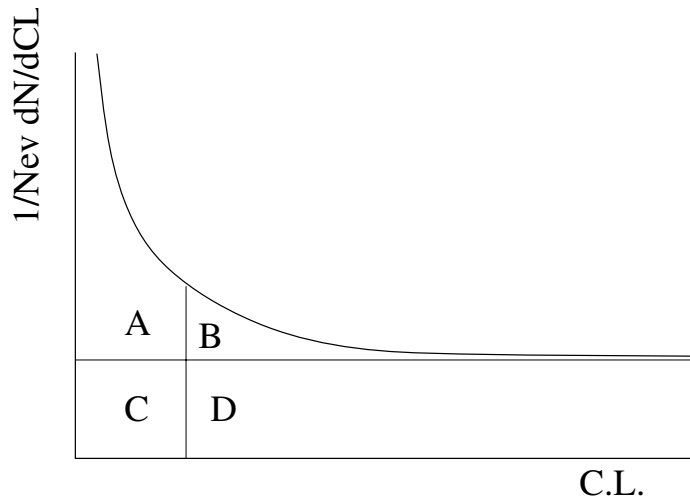

Figure 4.5: Confidence level distribution for the CPV–LEDA correlations. The horizontal line is a constant function, fitted to the distribution at high CL. The vertical line represents a CL threshold.

D The number of rejected charged particles, $N_{\mathrm{rej,ch}}$.

The number of particles that is accepted in our photon sample, N_{acc}, is given by the sum of the areas of A and C. Consequently, the fraction of erroneously rejected photons and accepted charged particles can now be determined for a given value for the confidence level threshold.

Figure 4.6 shows the observed confidence level distribution for hits with a measured energy above 250 MeV in central events. The shape of this distribution is consistent with our expectation, which was depicted in figure 4.5: a monotonically falling curve, which approaches a constant function for high confidence level. The value of the constant is important, as it describes the number of charged particles detected by the CPV. A first-order polynomial fit on the part of the graph with $CL > 0.55$ shows that the graph is indistinguishable from a horizontal line in this interval, within the statistical error. As can be seen from the fit parameters, this constant term can be estimated with a statistical error of about 3% for energies of 250 MeV and higher.

In figure 4.7, the effect of the contamination by charged particles is shown as a function of the $p_\perp$ of the recorded calorimeter showers. This plot is obtained by dividing the area of part C in figure 4.5 by the entire area below the given CL cut. Here it is observed that there is a peak of charged particle showers at

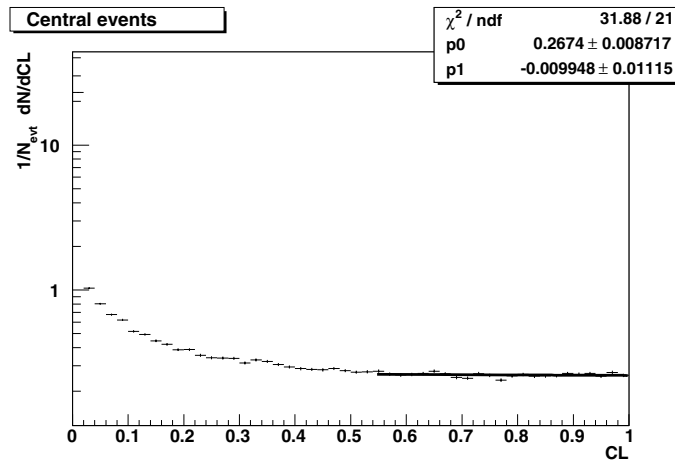

Figure 4.6: Confidence level distribution for the CPV–LEDA correlations for LEDA hits with an energy above 250 MeV, in central events. The horizontal line is a fit of the graph at high confidence level ($CL > 0.55$).

the apparent transverse momentum of $p_\perp < 0.25\,\mathrm{GeV}/c$. Above this value, the fraction of accepted hits that is caused by charged particles is approximately constant.

The CL cut to be used for the filtering of charged particles should be high enough to reject only few photons due to random correlation, but also low enough to reject the majority of charged particles. For various CL cuts, the contamination by charged particles and the fraction of rejected photons has been determined from the CL distribution. The results of this study are shown in figure 4.8 for our central sample. The cut that will be used is $\mathrm{CL}_{\mathrm{cut}} = 0.10$. With this cut, only about 3% of the photons is rejected. The photon spectra can now be corrected for the charged particle contamination shown in figure 4.7. This contamination is accurately known over the entire $p_\perp$ domain between 0.5 and $2.4\,\mathrm{GeV}/c$ for this CL threshold. The uncertainty introduced to the photon spectra from this correction is therefore less than 1%.

As the number of rejected photons is determined by the number of coincidental correlations between the veto detector and the spectrometer, it rises with the multiplicity of the event. The results for the peripheral class, which has a lower multiplicity, will therefore be better than those shown in figure 4.8. For

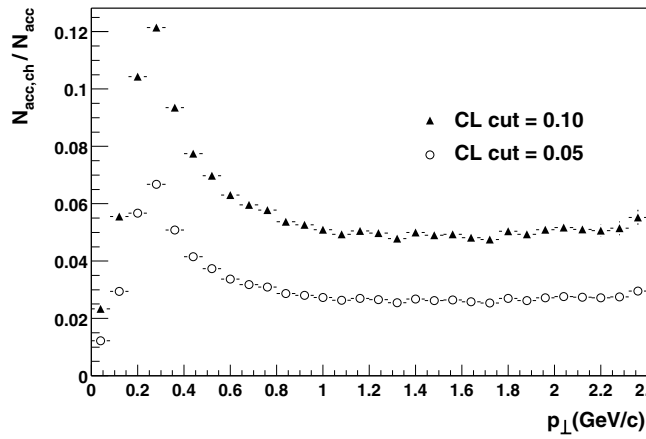

Figure 4.7: The contamination of the sample of accepted particles by charged particles, expressed as the fraction $N_{\mathrm{acc,ch}}/N_{\mathrm{acc}}$.

this class, our photon sample will therefore be more pure than that obtained for the central class, and the associated error will be smaller.

Figure 4.9 shows the ratio of actual photon production and observed photon production. This ratio contains both the effects of photon rejection and of contamination of the photon sample by charged particle hits. For high energies, this corrective factor appears to be independent of the energy. However, in the further analysis, the measured factor is used instead of the fitted constant function. This means that the error introduced by this correction is as large as the error on the individual points in figure 4.9. This error rises to about a percent for photon energies higher than 1 GeV.

4.4 Reconstruction efficiency

In the previous section, the effect of the filtering of charged particles by means of the CPV detector has been explained. The other important contribution to the photon measurement efficiency arises from the shower reconstruction. Because of the high multiplicity of hits in the LEDA detector, especially in the most central events, two photons will often hit the detector at locations close to each other. If the distance is smaller than a few times the size of one lead-glass module, their showers will overlap, and both photons will merge into a higher

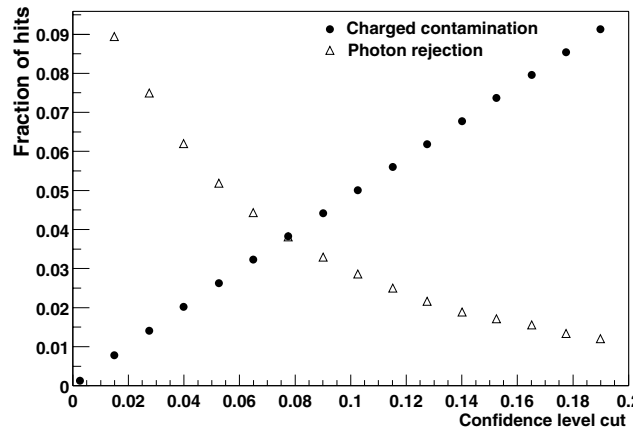

Figure 4.8: Rejected neutral hits and accepted charged hits as a function of the confidence level cut, for the central event class.

energy photon after clustering.

This effect of overlapping showers on the reconstruction efficiency can be determined by using measured data in the various centrality classes exclusively. The idea behind the procedure is to add a single photon shower to an unclustered measured event. By comparing the output of our clustering and selection routines for both the original and the modified event, the reconstruction efficiencies can be determined.

The method for calculating the reconstruction efficiency consists of the following steps:

1. The LEDA module signals of a peripheral event are clustered, using the method described in section 3.2.3. An isolated cluster without a corresponding CPV hit is selected to represent a single incoming photon, according to our selection criteria.

2. The LEDA signals of an event with a given centrality are grouped into clusters using this same clustering method, and the clusters that are associated with a hit in the CPV are removed. The resulting spectrum of this event is taken as the basis for the comparison later on.

3. The lead-glass module signals of the isolated photon shower of step 1 are added to the unclustered event used in step 2, at their original position in

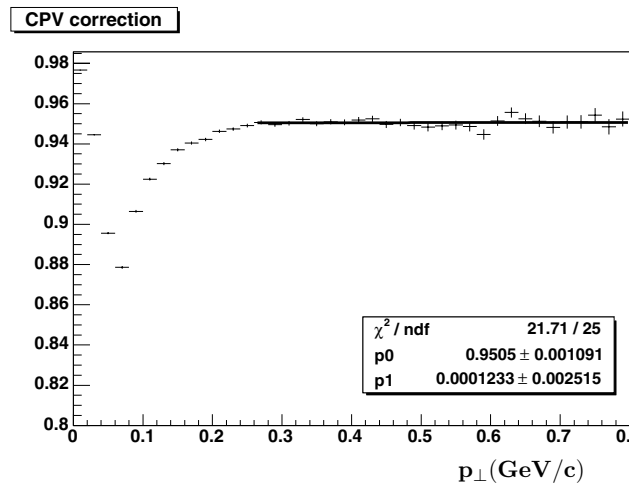

Figure 4.9: The multiplicative factor that has to be applied to the observed photon production with $CL > 0.1$ to obtain the actual photon production.

the detector. This step simulates the existence of an additional photon in the event. The effect of this addition on the global event characteristics (e.g. occupancy) is negligible.

4. The signals of the newly constructed event are again clustered and filtered for charged particles. The difference between the energy spectrum of this newly constructed event, and the original one is determined. From this difference, the photon reconstruction efficiency can be obtained.

Special care has to be taken to correct for an effect that artificially inflates the fraction of photons that overlap. For all photons in an event, the procedure as described takes into account the interaction with all other photons in that event, for a total of $N(N-1)$ interactions. However, this means all interactions are counted twice, as the real number of photon pairs is $\frac{1}{2}N(N-1)$. Overlap effects are therefore exaggerated by a factor of two if the above steps are followed. We have eliminated this effect by removing a newly created signal if its apparent energy was more than twice the energy of the photon added in step 3. In case of overlapping signals of two photons, this removes half of the overlap effect.

This procedure was repeated for about 1×10^7 photon showers for both the peripheral and the central event classes. It resulted in two spectra:

- the spectrum of all additional photons, added in step 3 of the procedure described above, and
- the difference of the spectra of the newly constructed events and the original events.

In the ideal case, in which there are no overlap effects and all photons can be measured individually, the latter spectrum is equal to the spectrum of the additional inserted photons.

The energy dependent photon reconstruction efficiency $\varepsilon(p)$ can now be determined; it is the ratio of the difference of the spectra of the original and the constructed events and the spectrum of the additional photons from the peripheral events.

4.4.1 Results of the efficiency determination

In figure 4.10 the reconstruction efficiencies for central and peripheral events are shown. As expected, the overlap effects are larger in the central events, in which the number of showers in the LEDA detector is much greater than in peripheral events.

For $p_\perp$ values above about $1\,\mathrm{GeV}/c$, the reconstruction efficiency of the central events rises above 1. This is the effect that two low-energy photons combine into one high-energy photon. As the number of photons falls exponentially with energy, this gives a relatively large contribution to the number of higher energy photons. Consequently, an efficiency higher than 1 can be encountered for high transverse momenta.

4.5 π^0 reconstruction efficiency

For our analysis, we need the ratio of the π^0 spectra of both our centrality classes (our so-called $f(p)$ function). The π^0 spectra that were used for our analysis were taken from the detailed WA98 analysis [23]. In this work, which will be summarized below, the π^0 spectra are determined using the two-photon invariant mass analysis described in section 2.4, which was also used in the measurement of the direct photon signal in [3].

Because the $f(p)$ function is determined by the π^0 spectra, and the $f(p)$ function occurs in the formula for the direct photon spectrum (4.4), the error in the π^0 spectra is an important component of the uncertainty in our final result. This contribution to the total error will be discussed in the next section, where

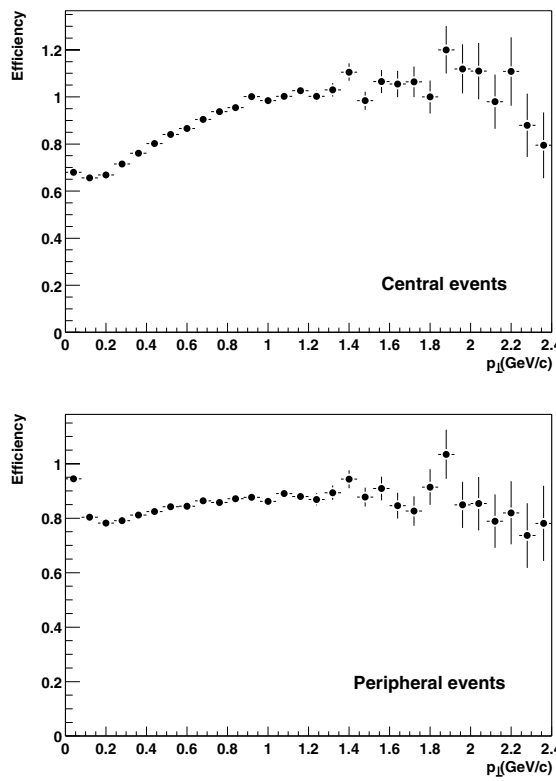

Figure 4.10: Photon reconstruction efficiency for central and peripheral events.

the $f(p)$ function is calculated. For this discussion we will use the results of different methods of calculating the π^0 spectra.

The number of π^0 that are measured in an invariant mass analysis depends on several factors besides the number of decayed π^0s, such as the detector response to the produced decay photons. Additionally, the selection of photons that are chosen as input for the invariant mass analysis also has an effect on the measured pion yield. A determination of the reconstruction efficiency of the π^0 produced in an event is therefore necessary. This π^0 reconstruction efficiency has been determined using simulated π^0 decays, in a procedure that is analogous to the measurement of the photon reconstruction efficiency.

A large number of single π^0 decay processes was simulated, and the decays with two photons in the acceptance range of the LEDA spectrometer were selected. These are the π^0s that correspond to the real π^0 signal that can be measured using an invariant-mass analysis on the experimental result.

For every selected simulated π^0, the spectrometer response for both decay photons was simulated using GEANT, and the resulting shower signals were added to the spectrometer signals of a measured event. This produced a new event, containing one additional π^0 signal. An invariant mass analysis was performed on both the original and the new event, and the $p_\perp$ spectrum of the photon combinations with an invariant masses within the range of the π^0 peak was determined. These spectra were summed over a large number of inserted π^0s with a specific transverse momentum, and divided to give the reconstruction efficiency for pions with that particular $p_\perp$.

The total π^0 reconstruction efficiency is the weighted average of the reconstruction efficiencies of the individual $p_\perp$ bins, with the weights given by the real π^0 spectrum. These weights are found in an iterative process, starting from the measured pion spectrum. The final neutral pion spectrum is shown in figure 4.12 for both our central and our more peripheral spectrum. This spectrum is obtained by an iterative process, starting from the measured π^0 spectrum. A detailed description of this method, which was also used for the earlier invariant mass analysis of the WA98 experimental data, can be found in [23].

One major factor influencing the reconstruction efficiency is the selection of spectrometer signals used for the invariant mass analysis. On the one hand, the combinatorial background is reduced if signals with a lower probability of being a photon are not used for the analysis, which may result in a more accurate determination of the content of the π^0 peak. These signals include for example wide showers, which are more likely to be produced by charged particles or by two overlapping photon showers. On the other hand, filtering out such signals will also remove some valid single photon showers, and therefore these strict

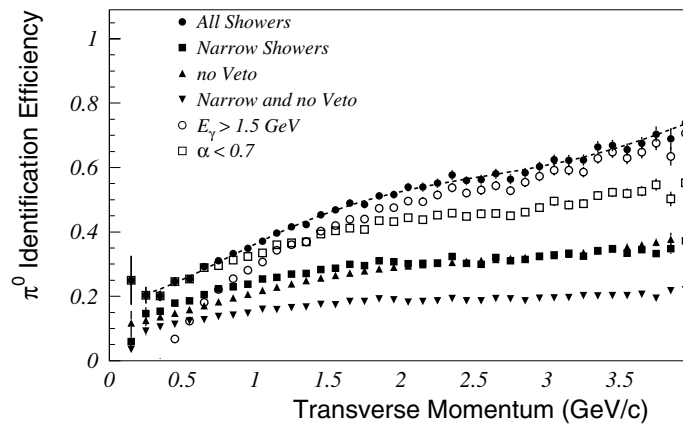

Figure 4.11: The π^0 reconstruction efficiency for central events, using various photon identification criteria. The selection of photon showers is based on the width of the shower; the presence of an accompanying hit in the veto detector; the energy of the shower; and shower-pair energy assymetry (denoted by $\alpha < 0.7$) (From [23])

criteria will result in a lower reconstruction efficiency.

Figure 4.11 shows the resulting π^0 reconstruction efficiency as a function of the π^0 transverse momentum for a number of photon identification methods. If all showers in the leadglass spectrometer are used for the invariant-mass analysis, the π^0 reconstruction efficiency increases with increasing transverse momentum. Part of this can be explained by overlap effects, and is similar to the way the photon efficiency rises above 1 in central events (see section 4.4).

To mimize overlap effects, a better identification of photon showers can be made, for example by only considering showers with a dispersion below a certain value. The π^0 reconstruction efficiency that is determined from this smaller selection of LEDA signals does not rise as much with increasing transverse momentum, which means that this method suffers less from overlapping showers. However, the total reconstruction efficiency gets much smaller. The invariant-mass analysis has also been performed using only showers with an energy above 1.5 GeV. This leads to a reconstruction efficiency that is slightly lower than without this threshold at higher $p_\perp$; however, at low transverse momentum, the reconstruction efficiency is very small.

Figure 4.11 shows the π^0 efficiency for central events. This is the worst case situation, as the π^0 identification efficiency depends strongly on the multiplicity of the event. The overlap effects are weaker in events in our peripheral event class, and the π^0 reconstruction is therefore better in the more peripheral events.

The π^0 spectrum is calculated by correcting the results of the invariant mass analysis for the reconstruction efficiency. Although the efficiency varies considerably for the different criteria in figure 4.11, the resulting π^0 spectra are comparable. For our analysis, however, it is not the π^0 spectra that are important, but the ratio of the spectra for our central and more peripheral event classes.

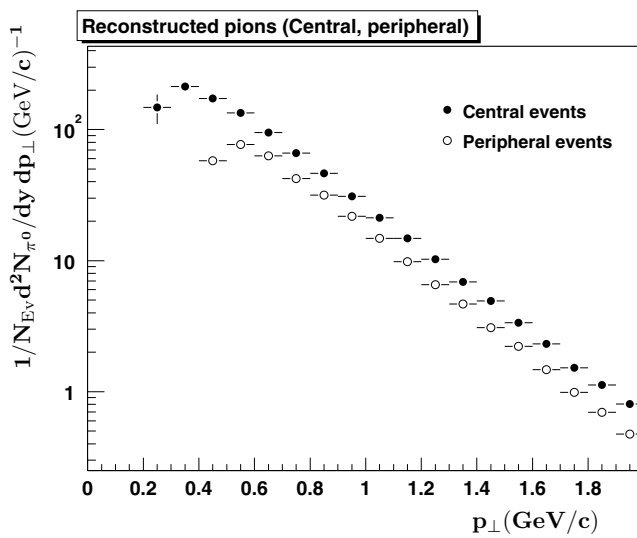

Figure 4.12: The π^0 yield for our central (closed circles) and our peripheral event classes (open circles). Only statistical errors are indicated. The systematic errors are discussed in section 4.6.

4.6 Determination of the $f(p)$ function

The function $f(p)$ as defined in equation (4.1) is determined from the reconstructed π^0 spectra for the two centrality classes used in our analysis, shown in figure 4.12.

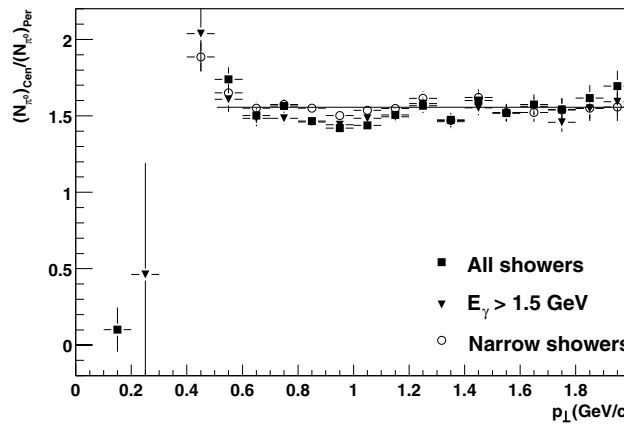

Figure 4.13: The ratio of the central and peripheral π^0 yield, $f(p)$, for several shower identification methods (described in [23]). The error bars are statistical only.

The resulting $f(p)$ function is shown in figure 4.13 for three photon identification criteria: all showers, narrow showers, and $E_\gamma > .15\,\mathrm{GeV}$. As can be seen in figure 4.11, these criteria result in the largest differences in the π^0 identification efficiency. The spread in the $f(p)$ calculated from these different photon identification criteria are a measure for the effect of the systematic errors in the π^0 reconstruction efficiency in our determination of the $f(p)$ function.

For a large $p_\perp$ interval, $f(p)$ is approximately constant. A fit of a linear function to all of the measured graphs in figure 4.13 above 0.5 GeV results in a value of 1.52 ± 0.46 for the constant term, and a negligible first order term $0.0163 \pm 0.35(\,\mathrm{GeV}/c)^{-1}$.

In the later analysis, we therefore use a constant function for $f(p)$. To estimate the correct error in $f(p)$, we can also look at the standard deviation of the distribution of all points above 0.5 GeV given in figure 4.14. This standard deviation of this distribution, 0.06, amounts to about 4% of the constant value of $f(p)$. As the systematic error on $f(p)$, we take a value of two times the standard deviation: 8 percent for $p_\perp > 0.6\ \mathrm{GeV}/c$. Below $0.6\ \mathrm{GeV}/c$, the systematic errors on the π^0 yields grow quickly, due to the large problems of the background subtraction and acceptance corrections at low momentum.

Our method of analysis is based on the equality of the central-to-peripheral ratio of the hadronic decay photons to $f(p)$. To check this equality, a phase

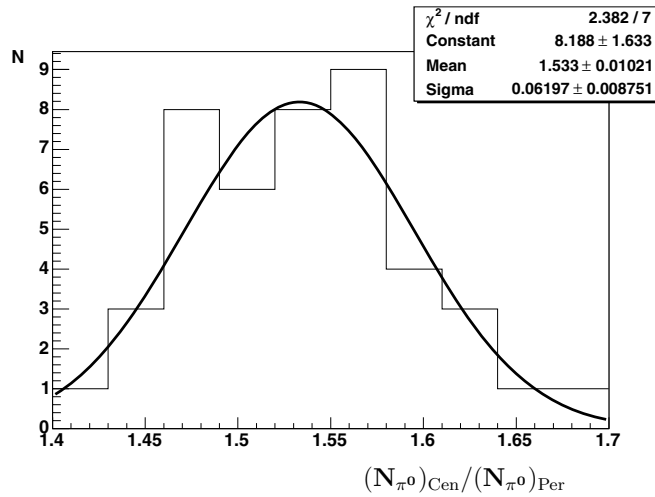

Figure 4.14: The distribution of all points in figure 4.13 between 0.5 GeV and 2 GeV.

space simulation was performed. This was based on the π^0 yield as measured by means of the invariant mass analysis. In the simulation, pions were produced according to this measured spectrum, assuming an isotropic momentum distribution. For these pions, an isotropic decay into two photons was simulated. After a geometrical acceptance cut on the photons, based on the actual detector setup, this resulted in a central and a peripheral photon spectrum.

The result of this simulation is shown in figure 4.15. It is clear that for $0.5\,\mathrm{GeV}/c < p_\perp < 2\,\mathrm{GeV}/c$ the ratio of central to peripheral photons is equal to the $f(p)$ function which is defined by the pion ratio. The systematic error introduced by the assumption that these two functions are equal can be estimated from the difference between the two graphs in figure 4.15, and is approximately 5%.

4.7 Neutron and anti-neutron background

Charged particles entering the LEDA spectrometer can be filtered by means of the CPV detector, as described in section 4.3.1. However, neutrons do not give a signal in the CPV, and cannot be seperated from photons in this way. The only way to filter out the neutron signals would be a selection based on the size and shape of the shower. As mentioned in section 3.2.2, showers produced by

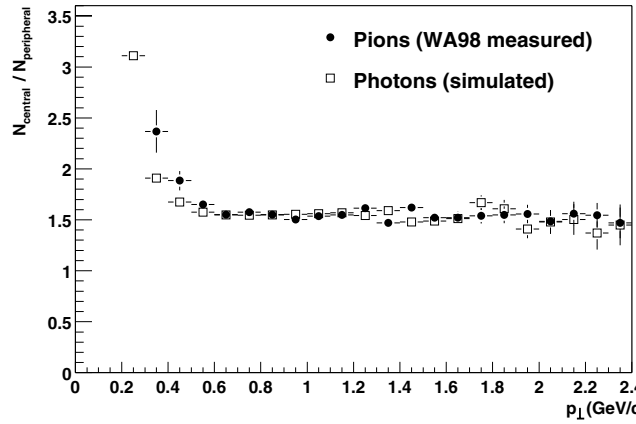

Figure 4.15: The ratio of hadronic decay photon yields from a phase space Monte Carlo simulation for the central and peripheral class, compared to $f(p)$.

neutrons are generally larger than those produced by photons. However, the size of photon showers varies considerably, and grows with the photon energy. Therefore, a cut on the shower size would have a $p_\perp$ dependent effect on the photon spectrum that would be difficult to determine.

Simulations using the GEANT package [24] in combination with the VENUS event generator [25] show that the number of neutrons entering the LEDA detector is larger than the number of charged pions over a large part of the p_T domain [3]. For $p_T > 2$ GeV/c the number of neutrons exceeds the number of π^+'s by an order of magnitude, and the number of anti-neutrons is almost equal to the number of π^+'s. However, these neutrons deposit only a small part of their energy in the lead-glass. This reduces the number of neutron and anti-neutron signals in the high p_T domain. Most of the neutron signals in the calorimeter fall below 500 MeV/c. The ratio of neutrons plus anti-neutrons to photons after taking the detector response into account is about 0.05 for the $p_\perp$ range under consideration ($0.5\,\mathrm{GeV}/c^2 < p_\perp < 2.0\,\mathrm{GeV}/c^2$).

From VENUS simulations it is seen that the number of produced neutrons and anti-neutrons is proportional to the proton and anti-proton yield. Results from the NA49 experiment [26] show that the $p + \bar{p}$ yield scales with the centrality of the collision in the same way as the pion yield. This implies that the ratio of central to peripheral $n + \bar{n}$ yield is equal to the same ratio for

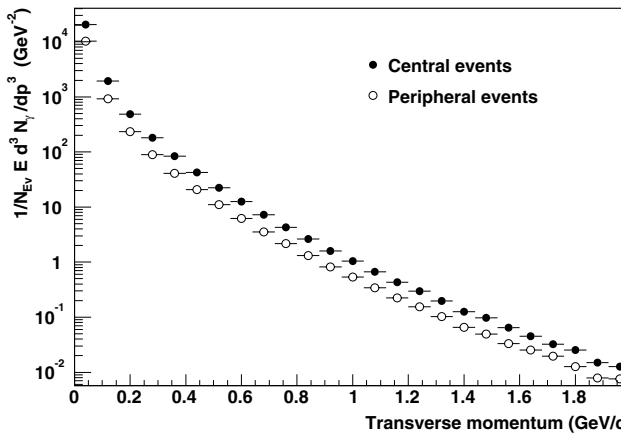

Figure 4.16: Observed photon spectra, corrected for reconstruction efficiency. Only statistical errors are included in the error bars.

pions, which we have called $f(p)$. Our method of extracting the direct photon signal is based on the subtraction of the $f(p)$ scaled peripheral spectrum from the central spectrum. In this subtraction, the neutron contribution will be strongly reduced, due to the cancelation of the largest part of the neutron signal in the central events by the neutron signal in the peripheral events. We will assume that the central and the peripheral neutron contributions will cancel completely in the calculation of the direct photon signal. At most, this means an error of 5% in the central photon spectrum, as that is the neutron contribution as mentioned above. Since the NA49 experiment has suggested a large degree of scaling between neutron and pion yield, we conservatively introduce an additional systematic uncertainty of 3% on the central photon spectrum.

4.8 The direct photon signal

Figure 4.16 shows the observed photon yield, corrected for the efficiency correction determined in section 4.4. Note that this figure only contains the statistical errors, which are very small. The acceptance of the photon detector has not been taken into account for this figure, and the absolute photon yield cannot therefore be determined from it. This is not very important for our method, as we will only use the ratio of the spectra of the two centrality classes.

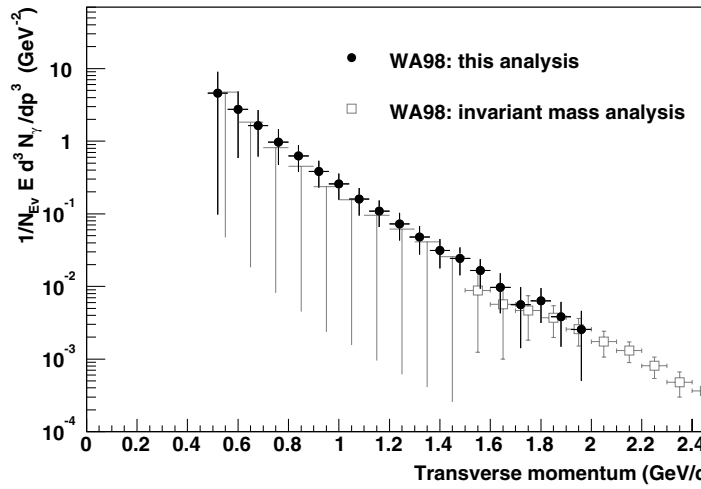

Figure 4.17: The result of the inclusive photon analysis, $\mathrm{Cen}_{\gamma d} - f(p) \cdot \mathrm{Per}_{\gamma d}$, compared to the direct photon yield as measured using the invariant mass analysis [3]. The error bars include the systematic errors, specified in table 4.2.

The final result, as defined by equation (4.4), is determined by subtracting the $f(p)$ scaled peripheral photon spectrum from the central photon spectrum. The result of this subtraction is shown in figure 4.17. Also shown in this figure is the result of the previous invariant mass analysis [3].

Our new result shows a good agreement with this earlier result for the overlapping momentum interval $1.5\,\mathrm{GeV}/c < p_\perp < 2.0\,\mathrm{GeV}/c$.

The sources of the systematic uncertainties are given in table 4.2. As most of these arise from uncertainties in the central and peripheral photon yields, the table contains percentages in terms of these photon yields. We were unable to measure some of these errors, and for those we have given a conservative upper limit, as discussed before. The uncertainties are summed in quadrature to give the total uncertainty in the direct photon spectrum.

In figure 4.18, the direct photon signal is compared to the systematic error. The points represent the measured photon spectrum in the central event class, expressed as a ratio of the spectrum predicted from the peripheral events, $f(p) \cdot \mathrm{Per}_\gamma$. The error bars on these points denote the sum of the (small) statistical error in the photon spectra and the uncertainties stemming from the photon

Errors on the photon spectra	
Charged particle background	1%
γ reconstruction eff.	0.5–10% (Central)
	2–10% (Peripheral)
Non-target background	$< 3\%$ (Peripheral)
Neutron background	3%
Heavy neutral mesons	3%
Errors on the function $f(p)$	
π^0 yield	8%
Equality of π^0 and γ ratios	5%

Table 4.2: The systematic uncertainties contained in the direct photon yield. When a range is given, the first number applies to $p_T \approx 0.7\,\mathrm{GeV}$, and the second number to $p_T \approx 2\,\mathrm{GeV}$.

reconstruction efficiency (see figure 4.10).

The measured direct photon yield integrated over the momentum domain $0.8\ \mathrm{GeV}/c < p_\perp < 1.5\ \mathrm{GeV}/c$ constitutes $(20 \pm 2 \pm 9)\%$ of the total photon production in central collisions, where the errors indicate the statistical and systematic uncertainties respectively.

It is clear that the inclusive photon method enables the extension of the measured direct photon signal down to a transverse momentum of about $0.5\,\mathrm{GeV}/c$. The spectrum in figure 4.17 is not necessarily equal to the central direct photon spectrum, as already indicated in section 4.1. However, if the assumption is made that the peripheral direct photon signal is negligible compared to the central one, the result can be compared to the predictions of several theoretical models. A number of these models will be the subject of chapter 5.

4.9 Interpretation of the result

In the previous section we assumed that the direct photon production in our peripheral sample was negligible compared to that in the central collisions. The outcome of the analysis is therefore properly considered to be a lower limit of the direct photon signal in central collisions. If there is a significant direct photon signal in our peripheral sample (which is not impossible, as we have chosen our so-called peripheral sample to be at relatively high E_T), our result is an underestimate of the central direct photon signal.

The spectrum that was shown in the previous section, here denoted by S,

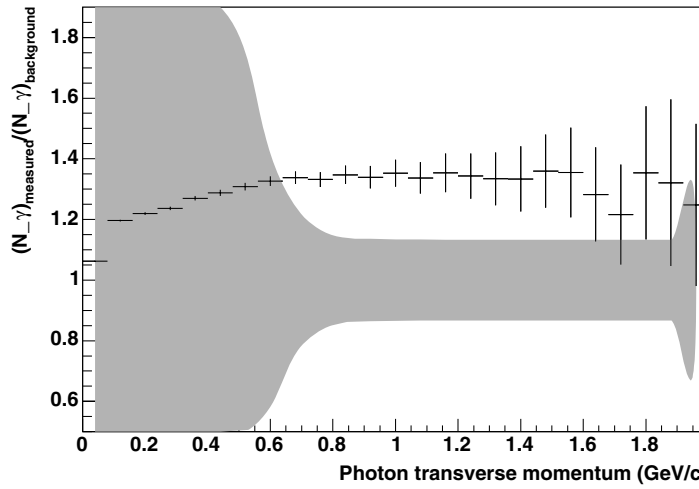

Figure 4.18: The measured photon spectrum in the central event class, expressed in terms of the background spectrum, $f(p)\mathrm{Per}_\gamma$. The shaded region represents the systematic errors, except for the error originating in the photon efficiency calculations, which is added to the statistical errors, and shown as error bars. The error coming from the uncertainty in $f(p)$ is included in the systematic error.

was calculated with the subtraction given on the left-hand side of equation (4.4). Using the right-hand side of (4.4), we can express the direct photon production in central events as

$$\mathrm{Cen}_{\gamma d} = S + f(p) \cdot \mathrm{Per}_{\gamma d}. \tag{4.9}$$

An upper limit of $\mathrm{Cen}_{\gamma d}$ is given by a high upper limit of $\mathrm{Per}_{\gamma d}$. We can make the assumption — likely incorrect — that the thermal conditions in peripheral collisions are identical to those in central collisions. The only difference in the direct photon yield is then caused by the size of the medium. In central collisions, a larger part of the nucleons take part in the collision, and the average number of collisions per participating nucleon is higher. The most conservative assumption, resulting in the strictest lower limit, is that the direct photon yield only scales with the number of participating nucleons. This number is given in table 4.1. The number of participants in peripheral collisions is on average 43% of the number of participants in central collisions. Combined with an $f(p)$

function of 1.557, we find an upper limit on the central direct photon yield of

$$\mathrm{Cen}_{\gamma d} = S \times \frac{1}{1 - f(p) * 0.43} = 2.96 \cdot S. \tag{4.10}$$

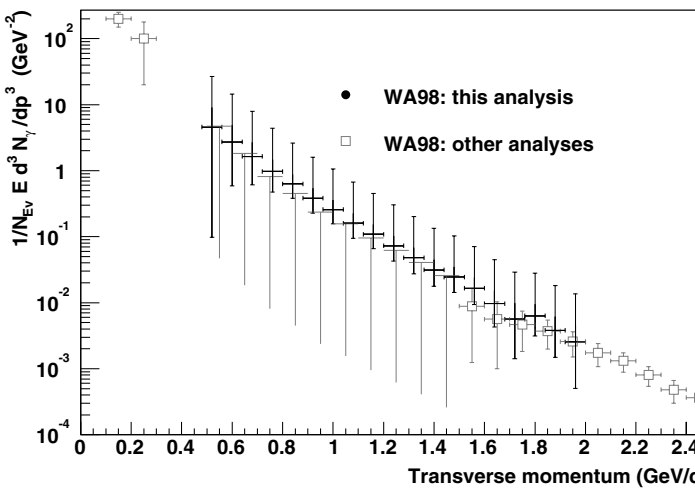

Figure 4.19: Upper and lower limits for the direct photon yield in central collisions. See the text for the definitions of these limits. The graph includes data from other analyses of the WA98 experimental data: a photon-photon HBT analysis at low transverse momentum, and the invariant mass analysis at higher momenta.

The upper and lower limits for the direct photon yield are shown in figure 4.19. The lower end of the error bars in this graph represent the 90% C.L. lower limit, making the assumption of an absence of direct photons in peripheral events. The upper end of the error bars show the 90% C.L. upper limit, assuming a direct photon production that is proportional to the number of participants, as described above. These limits can be compared with the results of the invariant mass analysis, also shown in the figure; for $p_T < 1.5\,\mathrm{GeV}/c$, these are also 90% C.L. upper limits.

Our results are consistent with the earlier invariant mass analysis results. From these two sets of results, we can conclude that the most likely values for the direct photon production are near the lower limits of our spectrum; this suggests a very low direct photon yield in our peripheral class of events.

Figure 4.19 also contains the result of a recent photon-photon HBT analysis [27], from which the direct photon emission at very low $p_\perp$ could be estimated. These HBT results are also consistent with the results of our analysis, although the large difference in the $p_\perp$ domains of the results and the large uncertainties in both results make it hard to draw concrete conclusions.

Chapter 5

Comparison with theory

In the previous chapter, the direct photon spectrum as observed in Pb–Pb collisions has been described. As explained in section 4.1, our analysis method does not directly provide the exact direct photon spectrum. Instead, the result presented in section 4.8 is a lower limit, and the difference with the actual spectrum is proportional to the direct photon yield in peripheral events. In this chapter, we will make the assumption that this peripheral photon yield is negligible and that our result can therefore be taken to be the central direct photon yield. The correspondence of our results with the upper limits of of the invariant-mass analysis (shown in figure 4.19) largely supports this assumption.

In section 5.2, a model of the evolving system will be given, based on a hydrodynamical model of the expanding fireball. The predictions of this model can be compared to the measured direct photon spectrum. This will be done in section 5.3.

Recently, more complex calculations have been performed, for example by Turbide et.al [28], and by Gelis et.al. [29]. These calculations will be discussed in section 5.3.1, and they will be compared qualitatively with the experimental results.

5.1 Direct photon production

5.1.1 Photon production in a QGP

In a QGP in thermal equilibrium, the main contributing processes to the photon production cross section are quark annihilation ($q\bar{q} \rightarrow \gamma g$) and gluon scattering ($gq \rightarrow q\gamma$). The Feynman diagrams for the leading terms in these processes are given in figure 5.1.

The cross sections of these two processes have been first worked out in [30].

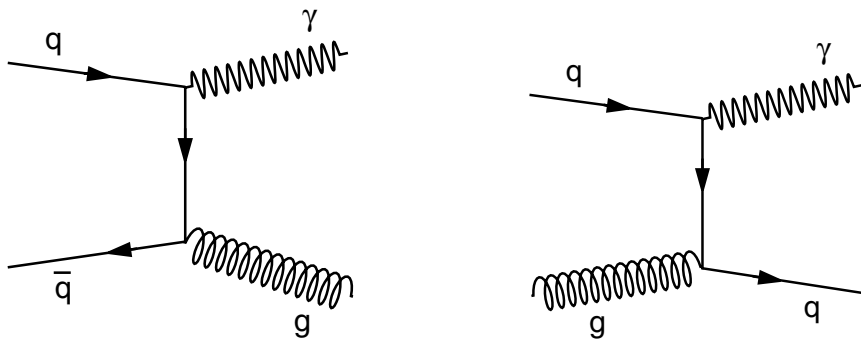

Figure 5.1: Leading order diagrams for photon production in a QGP: quark annihilation and gluon scattering

The contributions of both diagrams are of comparable magnitude, and summed together they result in the following expression for the direct photon production rate R at a photon energy E:

$$E\frac{dR}{d^3p} = \frac{5}{9}\frac{\alpha\alpha_s}{2\pi^2}\frac{T^2}{e^{E/T}}\log\left(\frac{2.912}{4\pi\alpha_s}\frac{E}{T}+1\right), \tag{5.1}$$

where T is the temperature of the system and α and α_s denote the electromagnetic and strong coupling constants, respectively.

In later work [31], several two-loop contributions to the photon yield were calculated:

$$E\frac{dR_2}{d^3p} = 0.0219\alpha\alpha_s T^2 e^{-E/T} + 0.0105\alpha\alpha_s ET e^{-E/T}, \tag{5.2}$$

where the first term describes bremsstrahlung, and the second term $q\bar{q}$ annihilation with an additional scattering in the medium[1].

These two-loop contributions turn out to be of the same order in α_s as the one-loop contribution. Calculations on the three-loop level have also been performed, also resulting in expressions of order α_s, and it is likely that the same holds for higher loop contributions [32]. This means that thermal photon production in the QGP cannot be described by a perturbative theory. However, as no better calculations are known, we will take the sum of (5.1) and (5.2) as the best available approximation of the photon production rate.

[1]The numerical constants in the expression given in [31] are too large by a factor 4, according to [17]. Equation (5.2) contains the corrected numbers.

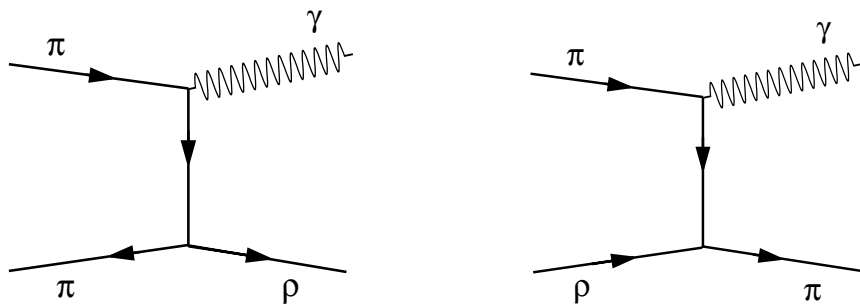

Figure 5.2: Leading order diagrams for photon production in a HG

5.1.2 Photon production in a hadron gas

The hadron gas (HG) phase that follows the QGP phase is also a source of direct photons. This phase is characterized by the interaction between mesons, and this is reflected by the Feynman diagrams of the leading photon production processes, as shown in figure 5.2. These processes are similar to those of the QGP, with the QGP constituents q and g replacing the π and ρ mesons, respectively.

The direct photon yield in a hadron gas was first calculated in [30]. Later calculations took into account the a_1 meson as intermediate particle in the reactions. The results of these calculations [17] can be parameterized as:

$$E\frac{dR}{dp^3} = 4.8\,T^{2.15}\,e^{-1/(1.35TE)^{0.77}}\,e^{-E/T}, \tag{5.3}$$

where E and T are given in GeV and the rate is in units of $\mathrm{fm}^{-4}\,\mathrm{GeV}^{-2}$.

As shown in figure 5.3, the production rate of the hadron gas is comparable both in shape and magnitude to the QGP production rate at the same temperature. Therefore, an interpretation of the measured photon production in a static model would not differentiate between the two states of matter. However, the yield in both HG and QGP is directly related to the temperature and the spatial volume of the system. This implies that the thermal photon spectrum provides a means to investigate the space-time evolution of the created system. A study of the temperature profile might provide an indication for the phase transition between the QGP and the HG.

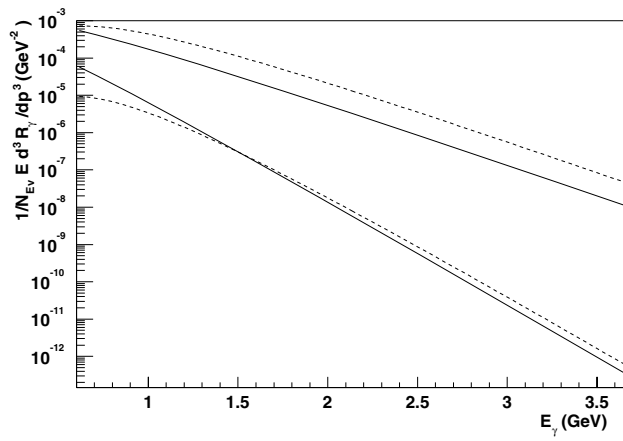

Figure 5.3: Direct photon production rate for $T = 150$ MeV (lower lines) and $T = 250$ MeV (upper lines). The dashed lines show the production rate of the hadron gas, equation (5.3), and the solid lines show the QGP rate given by the sum of equations (5.1) and (5.2).

5.2 Time evolution

The photon production rates in section 5.1 are given as a function of the temperature T. To calculate the integrated direct photon yield, which can be compared to the experimental results, it is necessary to calculate the time evolution of the temperature and volume of the system.

Figure 5.4 shows a space–time picture of the collision in the c.m.s. system. The two nuclei are Lorentz contracted, and travel with a velocity close to the speed of light along the z axis. As the system expands at relativistic velocities, the evolution is calculated in terms of the proper time τ in the local co-moving inertial frame of the plasma. After the collision at $t = 0$, a quark–gluon plasma is formed, provided that the energy density is sufficiently high. This formation phase will be followed by an equilibration phase. At the end of these phases, at proper time τ_0, the plasma is in equilibrium, and the subsequent evolution can be derived from hydrodynamical calculations.

Because of the expansion of the QGP, the temperature will decrease after τ_0, reaching a critical temperature T_c at a proper time of τ_c. At this temperature, a phase transition into a hadron gas occurs. We will assume a first order phase transition, during which the temperature will remain constant while the QGP

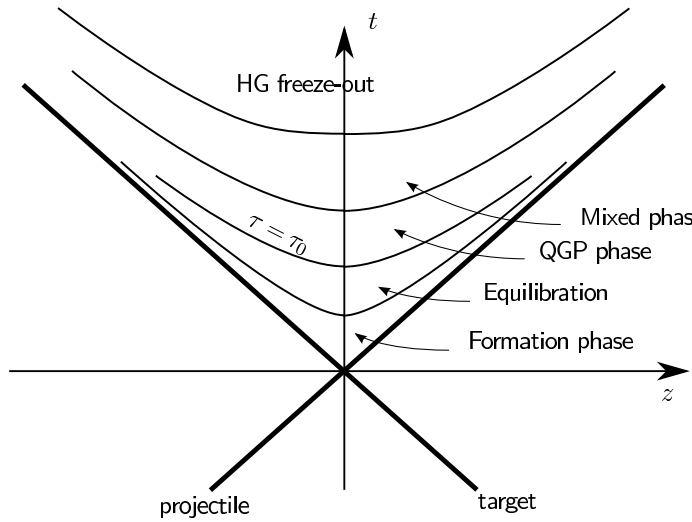

Figure 5.4: Space–time diagram of a heavy-ion collision

is converted to a hadron gas. At the end of this mixed QGP–HG phase at τ_h, the temperature will start to decrease again, eventually reaching the freeze-out temperature T_f at a time τ_f. After this time, the interactions between the hadrons cease, and the particles can escape freely. The thermal production of photons ends at this time as well. The evolution of the system is shown in figure 5.5 as a function of the local proper time τ.

To simplify our calculations, we will make a number of assumptions about the evolving system, following the Bjorken model [33]. Our first assumption is that the system shows a translational symmetry along the longitudinal (z) axis. This assumption can be justified by observed rapidity distributions dN/dy of produced particles. For high c.m.s. energies, the dN/dy distribution shows a plateau with a width of several rapidity units around mid-rapidity. This indicates that the properties of the system around $y = 0$ do not depend on the longitudinal coordinate z, and are a function of $x_\perp$ and τ only, where $x_\perp$ denotes the transverse coordinates.

Our second assumption is that the system will only expand in the longitudinal direction. In reality, there will also be an expansion in the transversal directions, but at a smaller magnitude. However, the longitudinal expansion is expected to dominate the thermodynamical evolution of the system.

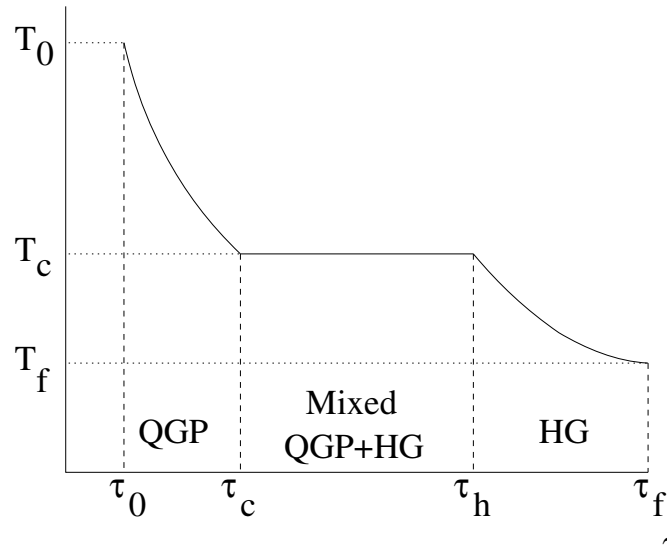

Figure 5.5: The temperature as a function of the proper time τ

The velocity of a particle due to the expansion of the system is given by

$$\frac{z}{t} = v_z = \frac{p_z}{E} = \frac{m_T \sinh y}{m_T \cosh y} = \tanh y. \tag{5.4}$$

From this equation and the definition of the proper time for that particle $\tau^2 = t^2 - z^2$, the coordinates t and z can be expressed in terms of y and τ:

$$z = \tau \sinh y, \qquad t = \tau \cosh y. \tag{5.5}$$

Our goal is to calculate the invariant photon production rate of the entire system, $E\, d^3N/dp^3$, by integrating the production rates per unit of space–time volume, given in section 5.1:

$$E\frac{d^3N}{dp^3} = \int E\frac{d^3R}{dp^3} d^4x \tag{5.6}$$

To do this, we need to rewrite the size of a space–time volume element,

$$d^4x = dt\, dz\, d^2x_\perp, \tag{5.7}$$

in terms of y and τ. The Jacobian of this transformation is given by

$$dt\, dz = \begin{vmatrix} \frac{\partial t}{\partial \tau} & \frac{\partial z}{\partial \tau} \\ \frac{\partial t}{\partial y} & \frac{\partial z}{\partial y} \end{vmatrix} d\tau\, dy = \tau, \tag{5.8}$$

and therefore the space–time volume element can be written as

$$d^4x = \tau d\tau\, dy\, d^2x_\perp. \tag{5.9}$$

where dy indicates the rapidity interval.

Because of the translational symmetry, the integration over the rapidity y is trivial, while in first approximation the integration over $x_\perp$ for a central collision results in a factor πR_A^2, where R_A is the radius of the colliding nuclei. The invariant direct photon yield in the QGP is therefore given by:

$$\begin{aligned} E\frac{d^3N}{dp^3} &= \int E\frac{d^3R}{dp^3}d^4x \\ &= \pi R_A^2 \int dy \int \tau d\tau E\frac{d^3R}{dp^3}. \end{aligned} \tag{5.10}$$

where $E\, d^3R/dp^3$ is the production rate, given in equations (5.1) and (5.2).

The Quark–Gluon Plasma Phase

In the Bjorken approximation, the temperature T depends on τ only, not on any spatial coordinate. In the QGP the quarks are considered to be nearly massless, which means that the QGP can be treated as an ideal relativistic gas. The expansion of the system is adiabatic, which implies that τT^3 is constant during the QGP phase. Therefore, the temperature of the plasma is given by

$$T(\tau) = T_0 \times \left(\frac{\tau_0}{\tau}\right)^{1/3}. \tag{5.11}$$

This can be substituted into the expression for the production rate (5.10), to give an integration over the temperature T. Using the expressions (5.1) and (5.2) for the direct photon rates, this yields

$$\begin{aligned} E\frac{d^3N}{dp^3} &= 3\pi R_A^2\, \Delta y\, T_0^6\, \tau_0^2 \int_{T_c}^{T_0} \int dT\, T^{-7} \left\{ \frac{5}{9}\frac{\alpha\alpha_s}{2\pi^2} T^2 e^{-E/T} \log\!\left(\frac{2.912E}{4\pi\alpha_s T} + 1\right) \right. \\ &\quad \left. + 0.0219\, \alpha\alpha_s\, T^2 e^{-E/T} + 0.0105\, \alpha\alpha_s\, ET e^{-E/T} \right\}. \end{aligned} \tag{5.12}$$

This integration is over the entire QGP phase, which covers the temperature interval between T_c and T_0.

The Mixed Phase

As soon as the temperature reaches the critical temperature T_c, the QGP starts to disappear, and the hadron gas phase starts to appear. For our massless

relativistic gas approximation, the proper time τ_c at which this happens is determined from equation (5.11):

$$\tau_c = \left(\frac{T_0}{T_c}\right)^3 \tau_0. \tag{5.13}$$

In our model, we assume that this phase transistion is first order. In this case, during this mixed phase, the temperature is constant: $T = T_c$. During the mixed phase, the fraction $f(\tau)$ of the matter that is in the QGP phase decreases from 1 at τ_c to 0 at τ_h. The direct photon production in the mixed phase is therefore given by:

$$\begin{aligned} E\frac{d^3N_{\text{mixed}}}{dp^3} &= \pi R_A^2\,\Delta y \int_{\tau_c}^{\tau_h} \tau d\tau \Bigg(f(\tau)\cdot E\,\frac{dN_{\text{QGP}}}{dx^4dp^3} \\ &\quad +(1-f(\tau))\cdot E\,\frac{dN_{\text{HG}}}{dx^4dp^3}\Bigg). \end{aligned} \tag{5.14}$$

The shape of the function $f(\tau)$ can be derived from the time evolution of the entropy density s of the system. During the mixed phase, s falls from a value of $s_{\text{QGP}}(T_c)$, the QGP value at the critical temperature, to $s_{\text{HG}}(T_c)$, the value for a hadron gas. At any proper time τ between τ_c and τ_h, s is given by

$$s(\tau) = f(\tau)s_{\text{QGP}}(T_c) + (1-f(\tau))s_{\text{HG}}(T_c). \tag{5.15}$$

Because the temperature is constant, s is given by

$$s(\tau) = s(\tau_c) \times \left(\frac{\tau_c}{\tau}\right)^{4/3}. \tag{5.16}$$

From these two equalities, it can be derived that

$$f(\tau) = \frac{1}{s_{QGP} - s_{HG}} \left(s_{QGP}\frac{\tau_c^{4/3}}{\tau^{4/3}} - s_{HG} \right), \tag{5.17}$$

where the entropies s_{QGP} and s_{HG} are evaluated at the temperature T_c.

The mixed phase ends when $f(\tau) = 0$. To calculate the length of this phase, we need values for the QGP and hadron gas entropies. These are proportional to the degeneracy number g, which depends on the degrees of freedom of the system. In a hadron gas, the degeneracy number g_{HG} is about 3, for the three kinds of pions that are the main constituents of the gas. In the QGP, the degeneracy number is much higher:

$$g_{\text{QGP}} = g_g + \frac{7}{8}(g_q + g_{\bar{q}}) = 8 \times 2 + \frac{7}{8} \times N_f \times N_c \times N_s \times 2, \tag{5.18}$$

where g_g is the number of gluons, and g_q and $g_{\bar{q}}$ the number of quark and anti-quark states. The number of colours N_f and the number of spin states N_s for the quarks are 3 and 2 respectively. The number of quarks flavours N_f in the gas is at least two, for up and down. With these numbers, the QGP degeneracy number is about 37. In that case, the end of the mixed phase occurs at $\tau_h \approx 7.16\tau_c$.

The Hadron Gas Phase

At the proper time τ_h, the system has been converted completely into a hadron gas and starts to cool down again. As before, the temperature is given by

$$T(\tau) = T_c \times \left(\frac{\tau_h}{\tau}\right)^{1/3}, \tag{5.19}$$

and an integral expression for the photon production in the hadron gas phase can be obtained analogously to eq. (5.12):

$$E\frac{d^3N}{dp^3} = 3\pi R_A^2\, T_c^6 \tau_h^2 \int_{T_f}^{T_c} dT\, 4.8 T^{-4.85} e^{-E/T-(1.35TE)^{-0.77}}, \tag{5.20}$$

with E and T in GeV and the production rate in $\mathrm{fm}^{-4}\,\mathrm{GeV}^{-2}$.

Summed together, equations (5.12), (5.14) and (5.20) give the total direct photon yield of a collision. This equation depends on three temperature parameters—the initial temperature T_0, the phase transition temperature T_c and the freeze-out temperature T_f—and four time parameters—τ_0, τ_c, τ_h and τ_f. However, of these parameters, the four time parameters are not independent. The parameters τ_c, τ_h and τ_f depend linearly on τ_0, which means that the value of τ_0 only influences the absolute normalization of the photon spectrum, and not the shape. In addition, the photon spectrum depends only weakly on T_f. In this model, there are therefore three quantities that that determine the photon spectrum: T_0, T_c, and a time scale.

5.3 Comparison of theory and experiments

As discussed in the previous section, the direct photon spectrum provides a probe for the time evolution of a heavy-ion collision. The shape of the spectrum contains information on the temperature of the system, and the yield puts contraints on the equilibration time. We can compare the predictions of the model with the experimental results found in section 4.8. These experimental results are given in the nucleus-nucleus c.m.s. frame, and can therefore be compared

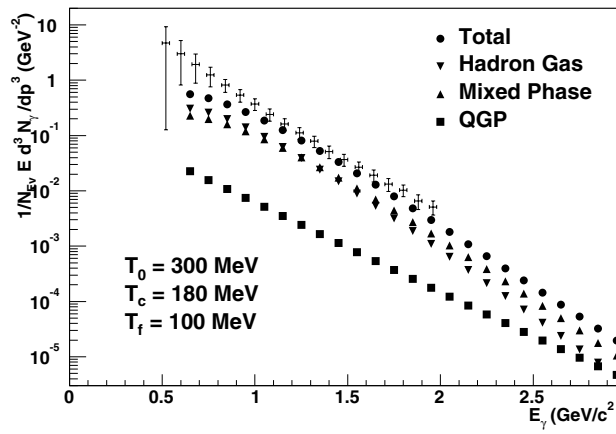

Figure 5.6: The observed direct photon spectrum compared with the outcome of a Bjorken model calculation. The entries with the error bars are our experimental results.

to the outcome of our model. Although hard scattering processes are also an important source of direct photons, we will first interpret the experimental data within the termal model described in the previous section.

Figure 5.6 shows the predictions of the Bjorken model using values for the parameters which are in agreement with the results of other experiments. As the figure shows, this simple hydrodynamical model can describe the experimental results reasonably well for $1\,\mathrm{GeV} < E_\gamma < 2.5\,\mathrm{GeV}$. The largest part of the photon yield is produced in the mixed and hadron gas phases.

The production yield of direct photons depends on the transverse dimension of the system, the rapidity interval in which the photons are emitted, and the formation time of the QGP. In the Bjorken approximation, which does not contain transverse expansion, the transverse dimension of the system is equal to the cross section of a lead nucleus, $\pi \times (7\,\mathrm{fm})^2$, in case of a central collision. For the rapidity interval Δy we take the LEDA detector rapidity coverage, which is about 0.8. If we take these values for the cross section and Δy, the normalization of the Bjorken model results in figure 5.6 corresponds to a reasonable formation time of $\tau_0 = 1.5\,\mathrm{fm}/c$.

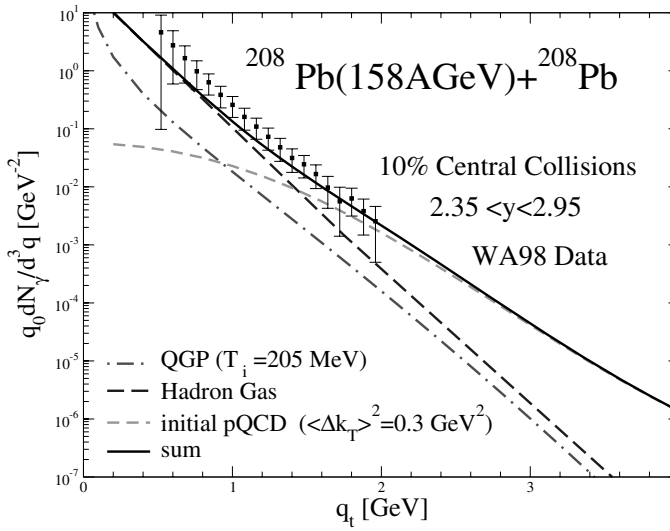

Figure 5.7: Decomposition of the thermal photon production into the contribution of the different sources, according to Turbide [36]. The points with error bars show the direct photon signal determined in our analysis.

5.3.1 Recent calculations

The interest in direct photon emission is demonstrated by the vast amount of (mainly theoretical) papers written on this subject. We referred to one of the most recent ones (Turbide et.al. [28]) in the previous section. This article gives a good overview of the available descriptions. Three competing sources are described that attribute to direct photon emission: primordial production in nucleon–nucleon collisions; thermal emission of the quark–gluon plasma; and thermal emission of a hadron source. Naively one expects the thermal emission to dominate at low q_T, and the contribution from nucleon–nucleon collisions at higher q_T.

The primordial nucleon–nucleon collision contribution is derived from the inelastic nucleon–nucleon cross section to produce photons, with additional broadening due to the Cronin effect. The amount of broadening is obtained by fitting p–A experimental data ([34], [35]). For the thermal components, several approaches are given.

The contribution of the different components at SPS conditions is shown in

figure 5.7. The calculations shown in this figure are for a rather standard fireball evolution (similar to the one we presented in this chapter) with $\tau_0 = 1$ fm/c, an initial plasma temperature $T_i = 205$ MeV, and a freeze-out temperature of $T = 120$ MeV, which is reached after a total lifetime of about 13 fm/c. As Turbide et.al. mention, the result of their calculations is consistent with the WA98 results from the invariant-mass analysis for an initial plasma temperature of 205 MeV. The largest contribution for $E_T > 1.5$ GeV is the initial pQCD component, produced by the primordial nucleon–nucleon collsions. The thermal contributions dominate in the E_T range below 1.5 GeV, where the invariant-mass analysis produced only upper limits for the direct photon yield. The Turbide calculation is also consistent with the results of our new analysis, which extends the direct photon yield into the region of low E_T. This implies that the low momentum direct photon component, which for the first tume is observed experimentally, can well be described by the emission from a thermalised hadron gas.

Calculations for non-equilibrium direct photon emission have only been performed recently for the higher bombarding energies of RHIC and LHC ([29], [37]). These calculations show possible contributions in the thermal E_T interval. Therefore, contributions from non-equilibrium processes to our direct photon observation cannot be ruled out.

5.4 Conclusion

In this chapter the Bjorken model of an expanding fireball has been explained. Several assumptions were necessary to apply this model to colliding nuclei:

- The system only expands in the longitudinal direction.
- The constituent quarks are massless, and the system can be treated as an ideal gas.
- The phase transition between a QGP and a hadron gas is first-order.

Using the expressions for photon production in a thermalized QGP and hadron gas, the direct photon production can be calculated for reasonable values of the initial temperature, critical temperature, hadronization temperature and space–time volume of the system.

Our results from the WA98 experiment can be explained in terms of this model. Assuming an initial temperature of 300 MeV and a critical temperature of 180 MeV, the results of the model correspond well to the measured spectrum for photon energies between 0.8 and 2 GeV.

The Bjorken model is a very simple model, and the production rates we used were likewise based on simple calculations. The results can be refined by including transversal expansion, more kinds of particles and particle masses. These extensions of the models will have some effects on the calculated photon spectrum. It has been pointed out [38] that the inclusion of heavier mesons can extend the lifetime of the hadron gas phase. This results in a larger fraction of the photons that is produced in the hadron gas phase, and a lower dependence of the direct photon signal on the temperature of the QGP.

At higher photon energies, the observed spectrum lies far above the results of the thermal model calculations. Comparison with experiments with smaller nuclei and pQCD calculations yield that the high-E_T tail of the spectrum can be explained by hard initial scattering between nucleons of the colliding Pb nuclei. However, the same pQCD calculations also show that for lower E_T, these hard initial scattering processes are insufficient to explain the observed spectrum; below 1 GeV, most of the direct yield has to come from thermal processes. This important low-momentum direct photon component could be determined for the first time from the analysis described in this thesis.

Bibliography

[1] NA50 collaboration. Phys. Lett. B, 477 (2000) 28.

[2] F. Antinori et al. Nucl. Phys. A, 663 (2000) 717c.

[3] M. M. Aggarwal et al. Phys. Rev. Lett., 85 (2000) 3595.

[4] N. J. A. M. van Eijndhoven. Nucl. Phys. A, 618 (1997) 330.

[5] WA98 collaboration. *Proposal for a Large Acceptance Hadron and Photon Spectrometer*. Technical Report SPLC/91-17, CERN, (1991).

[6] A. Baden et al. Nucl. Instr, and Meth., 203 (1982) 189.

[7] M. M. Aggarwal et al. Phys. Lett, B, 469 (1999) 30.

[8] A. Angelis et al. Nucl. Phys. A, 566 (1994) 605c.

[9] E. Iarocci. Nucl. Instr. and Meth. A, 217 (1983) 30.

[10] M. M. Aggarwal et al. Phys. Lett, B, 469 (1999) 30.

[11] T. C. Awes et al. Nucl. Instr. and Meth. A, 279 (1989) 479.

[12] G. Young et al. Nucl. Instr, and Meth. A, 279 (1989) 503.

[13] T. Peitzmann et al. Nucl. Instr. and Meth. A, 376 (1996) 368.

[14] B. Rossi. *High Energy Particles*. Constable, (1952).

[15] W. R. Leo. *Techniques for Nuclear and Particle Physics Experiments*. Springer Verlag, (1987).

[16] K. Reygers. Ph.D. thesis, University of Münster, (1999).

[17] F. D. Steffen and M. H. Thoma. Phys. Lett. B, 510 (2001) 98.

[18] W. Zajc et al. Nucl. Phys. A, 698 (2002) 39c.

[19] M. Aggarwal et al. Nucl. Phys. A, 685 (2001) 399.

[20] R. Glauber. In W. Brittin and L. Dunham, editors, *Lectures in Theoretical Physics*, volume 1, page 315. Interscience, New York, (1959).

[21] D. Kharzeev, C. Lourenço, M. Nardi, and H. Satz. Z. Phys. C, 74 (1997) 307.

[22] F. Geurts. Ph.D. thesis, Utrecht University, (1998).

[23] M. M. Aggarwal et al. nucl-ex/0006007.

[24] R. Brun, F. Bruyant, M. Maire, A. C. McPherson, and P. Zanarini. *GEANT - CERN Data Handling Division*. DD/EE/84–1, (1987).

[25] K. Werner. Phys. Rep., 232 (1993) 87.

[26] C. Blume et al. Nucl. Phys. A, 698 (2002) 104c.

[27] M. Aggarwal et al. Phys Rev. Lett., 93 (2004) 022301.

[28] S. Turbide, R. Rapp, and C. Gale. Phys. Rev. C, 69 (2004) 014903.

[29] F. Gelis, H. Niemit, L. Ruuskanen, and S. Rüsänen. Nucl-ph/0403040.

[30] J. Kapusta, P. Lichard, and D. Seibert. Phys. Rev. D, 44 (1991) 2774.

[31] P. Aurenche, F. Gelis, R. Kobes, and H. Zaraket. Phys. Rev. D, 58 (1998) 085003.

[32] P. Aurenche, F. Gelis, and H. Zaraket. Phys. Rev. D, 61 (2000) 116001.

[33] J. B. Bjorken. Phys. Rev. D, 27 (1983) 140.

[34] C. Wong and H. Wong. Phys. Rev. C, 58 (1998) 376.

[35] D. Srivastava. Eur. Phys. J. C, 22 (2001) 129.

[36] S. Turbide, R. Rapp, and C. Gale. Hep-ph/0408119v1.

[37] S. Bass, B. Müller, and D. Srivastava. Phys. Rev. C, 58 (1998) 376.

[38] J. Cleymans and S. Wheaton. University of Cape Town. Private communication.

Summary

The Quark Gluon Plasma (QGP) is a state of matter consisting of deconfined quarks and gluons. It is hypothesized to exist at high baryon densities and high temperature. These circumstances are only available for experiments in heavy-ion collisions, and even there the presence of the QGP cannot be measured directly. A number of possible signs of the QGP have been proposed, based on theoretical models of such a medium; some of the most promising are J/ψ suppression, heavy quark enhancement, and thermal dileptons. Several indications have already been detected in experiments at the SPS at CERN, but the evidence is still inconclusive whether the QGP has been seen.

This thesis discusses another good probe to search for the QGP: the direct photon signal of the QGP, which consists of the photons emitted in the early phases of a collision, partly in thermal processes. The direct photon spectrum is highly dependent on the thermal evolution of the medium. A phase transition from the QGP to hadronic matter will have a detectable effect on this thermal spectrum. The WA98 experiment has been designed to measure this signal from Pb+Pb collisions at a beam energy of 158 GeV per nucleon. For this purpose, the most important detector in the experiment is the large lead-glass calorimeter. Together with the charged particle detector placed in front, this detector enabled the measurement of the emitted photon spectrum.

Observation of the direct signal is complicated by the presence of a number of other photon sources during the collision. The most important other process is the decay of neutral mesons, especially π^0, in the later phases of the collision. The amount of photons produced in decays is several times higher than the thermal signal, that carries the information about the early stages of the event. One way that this background can be estimated is by an invariant-mass analysis, in which the invariant mass is calculated of all pairs of detected photons. For decay photon pairs, the invariant mass will be equal to the mass of the original meson. In this way, the production of π^0 and other mesons can be estimated, and the total decay spectrum can then be determined. This method of analysis requires a good knowledge of the acceptance of the used detectors and other

systematic effects. It has been performed for the WA98 experimental data, and a direct photon signal has been found for transverse momenta between 1.5 GeV/c and 3.5 GeV/c.

In this thesis, an alternative method is proposed to eliminate the decay photons from the detected photon signal. The method depends on the measurement of the photon spectrum for several centrality classes. In the most central collisions, all or almost all of the nucleons in the colliding nuclei participate in the collision, and the energy density of the formed medium will be high, while in the most peripheral collisions, only a few nuclei will participate, and the energy density of the medium will be much lower. The number of direct photons as a fraction of the total photon spectrum is therefore much higher in central events than in peripheral events. By subtracting the scaled peripheral photon spectrum from the central photon spectrum, the decay photon spectrum can be eliminated, and the remaining signal consists of direct photons only. Because this analysis uses the ratio of measured spectra at different centralities, it is less sensitive to number of systematic effects. For instance, the acceptance of the detector is a factor that occurs equally in both spectra, and this effect therefore largely cancels.

Our inclusive photon analysis has been performed on the photon data of the WA98 experiment. The results are encouraging: the systematic effects are indeed different from those of the standard invariant mass analysis. Using our method, it was possible to produce a direct photon spectrum for transverse photon momenta between 0.5 GeV/c and 2.0 GeV/c. A comparison of this spectrum with the earlier results shows a good correspondence at the overlapping transverse momentum interval.

The measurement of a direct photon signal at lower $p_\perp$ provides a good opportunity to study the thermal evolution of the collision, as calculations show that the direct photon spectrum is dominated by hard initial scattering at higher transverse momenta. Only at low $p_\perp$ can the thermal signal from the QGP and the hadron gas phase be detected. A simple hydrodynamical model first proposed by Bjorken is used to describe the expanding medium in the first moments after formation and equilibration. This shows that the direct photon signal that we found is compatible with an initial temperature of about 300MeV, and a transition temperature of 180 MeV. With these parameters, the model shows that most of the thermal photons originate in the QGP/hadron gas mix during the phase transition, or in the following hadron gas phase.

Samenvatting

Het Quark–Gluonplasma (QGP) is een aggregatietoestand die bestaat uit ongebonden quarks en gluonen. Men denkt dat deze toestand bestaat bij hoge baryondichteden en hoge temperaturen. Deze omstandigheden zijn alleen bereikbaar voor experimenten in zware-ionenbotsingen, en zels daar kan het bestaan van het QGP niet rechtstreeks gemeten worden. Er zijn een aantal tekenen van het QGP voorgesteld op basis van theoretische modellen van een dergelijk medium. Enkele veelbelovende signalen zijn J/ψ-onderdrukking, zware-quarktoename en thermische dileptonen. Een aantal van deze indicatoren is al waargenomen in experimenten bij de SPS op CERN, maar het bewijs voor de aanwezigheid voor het QGP is nog niet overtuigend.

Dit proefschrift bespreekt een andere geschikte methode om het QGP te zoeken: het directe-fotonsignaal van het QGP, dat bestaat uit de fotonen die in de vroge fasen van een botsing worden uitgezonden, gedeeltelijk in thermische processen. Het directe-fotonspectrum is sterk afhankelijk van de thermische ontwikkeling van het medium. Een faseovergang van het plasma naar hadronische materie heeft een waarneembaar effect op dit thermische spectrum. Het WA98 experiment was ontworpen om dit signaal te meten uit Pb+Pb-botsingen bij een bundelenergie van 158 GeV per nucleon. Voor dit doel was de belangrijkste detector in het experiment de grote loodglascalorimeter. Samen met de detector voor geladen deeltjes die ervoor geplaatst was, maakte deze detector de meting van het uitgezonden fotonspectrum mogelijk.

Het waarnemen van het directe signaal wordt bemoeilijkt door de aanwezigheid in een botsing van een aantal andere bronnen van fotonen. Het belangrijkste andere proces is het verval van neutrale mesonen, met name π^0, in de latere fasen van de botsing. De hoeveelheid fotonen die door vervallen geproduceerd wordt, is enkele malen hoger dan het thermische signaal, dat informatie verschaft over de vroege fasen van een botsing. Een manier waarop deze achtergrond geschat kan worden is een invariante-massa-analyse, waarin de invariante massa wordt berekend voor alle paren van gedetecteerde fotonen. Voor vervalsparen is deze invariante massa gelijk aan de massa van het

oorspronkelijke meson. Op deze manier kan de productie van π^0 en andere mesonen bepaald worden, en daarmee ook het totale vervalsspectrum. Deze analysemethode vereist een goede kennis van de acceptantie van de gebruikte detector, en van andere systematische effecten. De analyse is uitgevoerd voor de data uit het WA98 experiment, en een direct-fotonsignaal is gevonden voor $1.5\ \mathrm{GeV}/c < p_\perp < 3.5\ \mathrm{GeV}/c$.

In dit proefschrift wordt een alternatieve manier voorgesteld om de vervalsfotonen te verwijderen uit het waargenomen fotonsignaal. Voor deze methode wordt het fotonspectrum gemeten voor verschillende centraliteitsklassen. In de meest centrale botsingen nemen alle of bijna alle nucleonen van de botsende atoomkernen deel aan de botsing, en de energiedichtheid van het gevormde medium zal hoog zijn, terwijl in de meest perifere botsingen slechts een paar nucleonen deelnemen, en de energiedichtheid veel lager zal zijn. Het aantal directe fotonen als een fractie van de totale fotonproductie is daarom veel hoger in centrale botsingen dan in perifere botsingen. Door een geschaald perifeer fotonspectrum af te trekken van een centraal fotonspectrum kunnen nu de vervalsfotonen verwijderd worden, en het overblijvende signaal bestaat dan enkel uit directe fotonen. Omdat deze analyse de verhouding tussen gemeten spectra bij verschillende centraliteiten gebruikt, is ze minder gevoelig voor bepaalde systematische effecten. Zo is bijvoorbeeld de detectoracceptantie een factor die in beide spectra meespeelt; dit effect kan in de verhouding weggestreept worden.

Onze inclusieve-fotonanalyse is uitgevoerd op de gegevens over de fotonen uit het WA98 experiment. De resultaten zijn veelbelovend: de systematische effecten verschillen voor deze analyse inderdaad van die van de standaard invariante-massa-analyse. Met onze methode was het mogelijk om een directe-fotonenspectrum te produceren voor $0.5\ \mathrm{GeV}/c < p_\perp < 2.0\ \mathrm{GeV}/c$. Een vergelijking met het eerder gemeten fotonenspectrum laat een grote overeenkomst zien voor het overlappende $p_\perp$-interval.

De meting van een directe-fotonensignaal bij lagere $p_\perp$ biedt gelegenheid om de thermische evolutie van de botsing te bestuderen, aangezien berekeningen laten zien dat het directe-fotonenspectrum by hoge $p_\perp$ gedomineerd wordt door harde initiële verstrooiing. Alleen bij lage $p_\perp$ kan het thermische signaal van het QGP en de hadrongasfase waargenomen worden. Een eenvoudig hydrodynamisch model dat oorspronkelijk is voorgesteld door Bjorken hebben we gebruikt om het uitzettende medium in de eerste momenten van de botsing na de formatie en equilibratie te beschrijven. Dit model laat zien dat het gemeten directe-fotonensignaal verklaard kan worden met een initiële temperatuur van ongeveer 300 MeV en een faseovergangstemperatuur van 180 MeV. Met deze parameters worden in het model de meeste thermische fotonen geproduceerd in het

QGP/hadrongas-mengsel gedurende de faseovergang, of in de daaropvolgende hadrongasfase.

Dankwoord

Ik ben blij dat mijn promotieonderzoek uiteindelijk toch afgerond wordt met dit proefschrift, omdat dat me de gelegenheid biedt om iedereen te bedanken die mij de afgelopen jaren heeft bijgestaan.

In de eerste plaats wil ik Nick van Eijndhoven bedanken. Tijdens mijn onderzoek heeft hij mij geholpen met de ontwikkeling van de analysemethoden, het schrijven van de benodigde software, en het begrijpen van de uitkomsten, maar waar ik de beste herinneringen aan heb zijn de avonden in Genève, waar hij de beste restaurants kende. Ik denk met veel plezier terug aan alle verhalen over zijn tijd op CERN.

René Kamermans heeft ook een belangrijke rol gespeeld in de tonstandkoming van dit boekje. Vooral in de laatste jaren, toen ik niet meer mijn volle aandacht aan het schrijven van mijn proefschrift kon besteden, heeft René mij intensief begeleid. Ook als ik af en toe een tijd niets van mij liet horen, bleef hij altijd optimistisch; dat dit boekje er nu eindelijk is, heeft daar zeker mee te maken.

Thomas Peitzmann en Paul Kooijman wil ik bedanken voor de waardevolle feedback die ik van hen heb gekregen op de conceptversie van dit proefschrift.

Dat ik zulke goede herinneringen aan mijn verblijf bij SAP heb, komt onder andere door de kamergenoten die ik gedurende die tijd heb gehad. Met Peter van de Ven, Nick van Remortel, Garmt de Vries, Peter de Rijke en Maaike Hersevoort heb ik voor korte of lange tijd mijn kamer in het Robert Van de Graaff of het Buys Ballot gedeeld. Ik hoop dat jullie het net zo naar jullie zin hebben gehad als ik.

Ook de andere collega's binnen SAP wil ik bedanken voor de goede tijd, zowel de vaste medewerkers en de secretaresses, als de promovendi, studenten en een enkele post-doc. De lunchgesprekken (eerst vooral over FC Utrecht, later meer over de Teletubbies en over The Sound of Music), de koffiepauzes, de tourpool... Jammer genoeg kan ik mij van de jaarlijkse kerstlunches niets meer herinneren, maar die schijnen ook wel erg gezellig geweest te zijn.

Ongeveer gelijk met het begin van mijn promotieonderzoek ben ik op kamers

gaan wonen. Dat ik dat overleefd heb, is te danken aan mijn huisgenoten Bartjan van Tent en Remko Stuik. Ik mis de gezamenlijke maaltijden, Starcraft, en de niet altijd even serieuze gesprekken. Ook Erik Molekamp, Han Monsees en Thom Zwagers hebben voor de nodige ontspanning gezorgd; met hun heb ik menig partijtje tafeltennis gespeeld, zowel op de universiteit als thuis op de achterkamer. Ik hoop dat we nog wel eens een keertje met z'n allen gaan snookeren of karten.

Mijn collega's op het CBS hebben de laatste jaren vaak belangstelling getoond voor mijn proefschrift. Ongetwijfeld is het voor jullie net zo'n verrassing dat het toch nog gelukt is als voor mij.

Op het allerlaatste moment voordat het manuscript naar de drukker ging heeft mijn zus een spelfout uit de uitnodiging gehaald. Machteld, bedankt!

En de laatsten die ik wil bedanken zijn tegelijk de belangrijksten. Mijn promotie was soms zwaar, en zonder de voortdurende steun van mijn ouders had ik het waarschijnlijk niet met succes afgerond. Pap, mam: bedankt voor alles wat jullie voor mij gedaan hebben.

Curriculum vitae

Ik ben geboren op 31 juli 1974 in Amersfoort. Van jongs af aan was ik geïnteresseerd in sterrenkunde en aanverwante onderwerpen, en nadat ik in 1992 mijn gymnasiumdiploma gehaald had aan het Corderius College in diezelfde stad, ben ik dan ook natuur- en sterrenkunde gaan studeren in Utrecht. Na mijn propedeuse werd mijn belangstelling gewekt voor de theoretische natuurkunde, en heb ik dus de sterrenkunde gedag gezegd. Mijn afstudeerscriptie, dat over veldentheorie op de lichtkegel ging, heb ik geschreven aan de vakgroep Theoretische Natuurkunde. Mijn doctoraal haalde ik in november 1997, waarna ik meteen als OiO aan de slag ging in de vakgroep Subatomaire Fysica.

In het kader van mijn promotieonderzoek heb ik deelgenomen aan zomerscholen in Nieuwpoort (België) en Kerkrade, en aan conferenties in Bergen (Noorwegen), Budapest en New York. Ook heb ik enkele keren CERN bezocht, waar het experiment is uitgevoerd waarvan ik data heb geanalyseerd. Het resultaat daarvan ligt nu voor u in de vorm van dit proefschrift.

In 2002 ben ik bij het Centraal Bureau voor de Statistiek aangenomen. Ik ben daar begonnen als trainee bij de taakgroep Methodologie en later bij Energie. Sinds eind 2003 werk ik met veel plezier bij de taakgroep Wetenschap en Technologie, waar ik me sinds kort bezig houd met econometrisch onderzoek aan het verband tussen productiviteit, innovatie en ICT-gebruik.